Article

Not peer-reviewed version

Petrogenesis and Provenance of the Triassic Metasedimentary Succession in the Sakar Unit, Bulgaria: Constraints from Petrology, Geochemistry and U-Pb Detrital Geochronology

Tzvetomila Vladinova * and Milena Georgieva

Posted Date: 2 July 2025

doi: 10.20944/preprints202507.0182.v1

Keywords: metasedimentary rocks; petrology; geochemistry; geochronology; Sakar unit; Bulgaria

 doi:10.20944/preprints202507.0182.v1

Article

Petrogenesis and Provenance of the Triassic Metasedimentary Succession in the Sakar Unit, Bulgaria: Constraints from Petrology, Geochemistry and U-Pb Detrital Geochronology

Tzvetomila Vladinova [1,*] and Milena Georgieva [2]

[1] Department of Geochemistry and Petrology, Geological Institute of the Bulgarian Academy of Sciences, 24 Acad. G. Bonchev Str., 1113 Sofia, Bulgaria

[2] Department of Mineralogy, Petrology and Economic Geology, Sofia University "St. Kliment Ohridski", 15 Tzar Osvoboditel Blvd., 1504 Sofia, Bulgaria

* Correspondence: tz_vladinova@geology.bas.bg

Abstract

This study investigates the Terrigenous-carbonate Sakar-type Triassic (TCSTT) and Sakar-type Triassic (STT) metasedimentary successions in the Sakar Unit, SE Bulgaria. Both share lithological similarities (alternation of carbonate-silicate schists, mica schists, marbles, and impure marbles) and are affected by post-Triassic metamorphism, but exhibit differences in metamorphic grade and provenance. The STT displays a higher metamorphic grade (low amphibolite facies) compared to the TCSTT (low greenschist facies). Petrographic observations and geochemical analyses indicate protoliths composed of arkosic sandstones, shales, and limestones, derived from a quartz-dominated source with minor contributions from intermediate magmatic sources. U-Pb geochronology of detrital zircons reveals a dominant Carboniferous age, supplemented by early Ordovician ages, consistent with the presence of Carboniferous-Permian magmatic rocks in the basement. The presence of Early Paleozoic and Cambrian-Neoproterozoic zircons in the detrital zircon populations suggests that older rocks in the basement of the Sakar Unit and Srednogorie zone are also sources of the sedimentary material. Based on immobile trace elements contents and discrimination diagrams, the siliciclastic component comes from rocks formed in a continental arc tectonic setting. REE patterns exhibit a negative Eu anomaly, inherited from the granitic source rocks.

Keywords: metasedimentary rocks; petrology; geochemistry; geochronology; Sakar unit; Bulgaria

1. Introduction

The bulk element composition of clastic sedimentary rocks constitutes a fundamental proxy for paleogeographic reconstruction and the elucidation of tectonic regimes of sediment deposition [1]. These lithological archives exhibit a good sensitivity to provenance characteristics and the physicochemical parameters of the depositional environment [2,3]. Provenance-sensitive geochemical indicators, exemplified by U-Pb geochronology of refractory detrital zircon, give robust constraints on sediment source terranes and the maximum depositional age of the strata [4]. The inherited geochemical signatures of metasedimentary rocks are linked to the compositional features of the source rocks and the imposed metamorphism [5]. The conservative behavior of specific trace elements during metamorphism provides a basis for lithostratigraphic correlations and petrogenetic interpretations [6-8 and references therein]. Redox-sensitive geochemical proxies offer critical insights into paleoenvironmental oxidation-reduction potentials, while protolith-sensitive geochemical indicators facilitate the characterization of the compositional attributes of the precursor lithologies.

 doi:10.20944/preprints202507.0182.v1

Carbonate geochemistry and particularly water-soluble trace elements are sensitive to water composition, physiochemical parameters of deposition, and carbonate mineralogy [9,10]. The contents of Sr, Rb, Ba, Mn, and REE are important geochemical indicators for carbonate origin and evolution. Sr/Ca ratio changes during authigenesis-diagenesis processes [11,12], Mn content reflects marine redox-oxidized conditions [13], and Mn/Sr ratio tracks post-depositional changes [14]. The $^{87}Sr/^{86}Sr$ isotope ratio could precisely determine the time of carbonate formation e.g., [15]. REE-Y patterns, including Ce and Eu anomalies, mirror the composition and oxidized-redox conditions of the seawater and are generally diagenetically stable [13, 16-17 and references therein]. Modern research indicates that variations in major elements (e.g., Fe_2O_3/Al_2O_3, MnO/Al_2O_3) and immobile trace element ratios (e.g., Ce/Ce*, Eu/Eu*, La_N/Ce_N, La_N/Yb_N, Nd_N/Yb_N, Sm_N/Yb_N) in seawater are significantly influenced by the plate tectonic setting of the depositional basin. These geochemical proxies offer valuable insights into the reconstruction of ancient plate tectonic environments and long-term changes in seawater chemistry [18,19]. However, post-depositional recrystallization processes can alter or obscure original sedimentary textures and primary geochemical signatures, thereby complicating the interpretation of such data [20,21].

In this paper, we combine a detailed petrographic observation, whole-rock geochemistry, and LA-ICP-MS U-Pb ages of detrital zircons in metasediments from the Sakar unit on Bulgarian territory, in order to trace the evolution of the sedimentary basin and to identify the source of the sediments and age of deposition. The parametamorphic sequence under investigation, exhibiting a lithology from pure silicicate to pure carbonate rocks, affected by metamorphism ranging from greenschist to amphibolite facies [22,23]. Prior research efforts have predominantly concentrated on the eastern Sakar-type Triassic (STT), whereas the western Terrigenous-carbonate Sakar-type Triassic (TCSTT, [24]) remains comparatively under-investigated. Trace elements geochemical datasets and detailed petrographic observation remain limited [22], and metamorphic P-T modeling has been primarily confined to the eastern Sakar Unit [25]. The absence of a universally accepted subdivision of the SSZ considers the westernmost rocks to be part of it [26]. The evident paucity of comprehensive investigations within the western Sakar Unit underscores the imperative for novel, foundational research endeavors. Furthermore, the acquisition of supplementary, high-resolution data from the eastern counterpart will facilitate a more robust lithostratigraphic and tectonothermal correlation between these geographically contiguous units, thereby enabling a more definitive assessment of their potential genetic affiliation or independent evolutionary trajectories through integrated, multi-proxy analytical approaches.

2. Geological Setting

The Sakar-Strandzha zone was considered as part of Srednogorie zone [24], Sakar-Strandzha zone (SSZ, [27,28]) or Strandzha zone [22,29]. In the context of the latest geological mapping, the Sakar unit is part of the Thracian lithotectonic unit [30]. The latter comprises the low-grade metamorphic rocks between the Rhodope massif and Srednogorie zone, affected by deformation along the Maritza shear zone and intrusion of Late Cretaceous plutons [31]. The uncertainty regarding the tectonic position of the SSZ is primarily due to the limited rock exposures. The SSZ rocks are covered by Tertiary sediments, which significantly hinder the detailed field and structural studies. Moreover, the complex geological history of the region, characterized by multiple phases of deformation and metamorphism, further complicates the interpretation of the tectonic evolution of the SSZ. In this paper, we will regard STT and TCSTT as part of the SSZ of Ivanov (2017) that is composed of Sakar and Strandzha units.

The SSZ occupies the SE part of Bulgaria (Figure 1a) and NW Turkey. It was either considered part of the Internal Balkanides and the Variscan orogen in SE Europe [27]. In Turkish literature, the SE part of SSZ is known as Strandja massif e.g., [32–36] and is regarded as westermost part of external Pontides with prominent Cimmerian structures. The SSZ is composed of Palaeozoic metamorphic basement, uncomformably overlained by thick Triassic-Jurassic metasedimentary cover, and Eocene to Quaternary sedimentary rocks [22,24,27–29,32,37], (Figure 1b). The Palaeozoic metamorphic

 doi:10.20944/preprints202507.0182.v1

basement (paragneisses, amphibolites, mica gneisses and schists) locally preserves remnants of Neoproterozoic metagranites [38–40]. Metagranitoids and gneisses in the basement of SSZ on the Turkish territory have late Pleozoic protoliths [32,38,41]. The basement is intruded by Permian and late Carboniferous metagranitoids [28,32,37,42–44]. Sakar granite batholith is the biggest late Palaeozoic intrusion (~ 300 Ma, [28,44,45]. Several metagranitoid complexes to the east of it also yield crystallisation ages between 230 and 312 Ma [28,46]. The subduction-related Late Palaeozoic magmatism coincides with a high-grade metamorphic event. This Variscan high-grade metamorphic event is characterised by zircon ages of 271 Ma [32] and 317 ± 3 Ma [47], complemented by structural data spanning 309 ± 24 to 257 Ma [48] in Turkey. This metamorphic event is constrained in the Bulgarian part by zircon rims yielding ages of 334 ± 3 Ma [40] and 327 ± 2 Ma [49], corroborated by structural evidence indicating maximum metamorphic age of 319 Ma [50]. These findings suggest a widespread and temporally diachronous metamorphic event across the region. The interpretation of the wide-spead magmatism in the area is also distinct—two separate events [46] or unified late Palaeozoic-early Mesozoic tectono-magmatic cycle based on similar geochemical signatures of the granitoids [51]. This suggests a transition from Permo-Triassic post-collisional magmatism to subsequent rifting and formation of a back-arc basin [52]. Continental sedimentation within this basin started as early as the Carboniferous-Permian, coinciding with the subduction and progressive consumption of the Paleotethys oceanic crust [22].

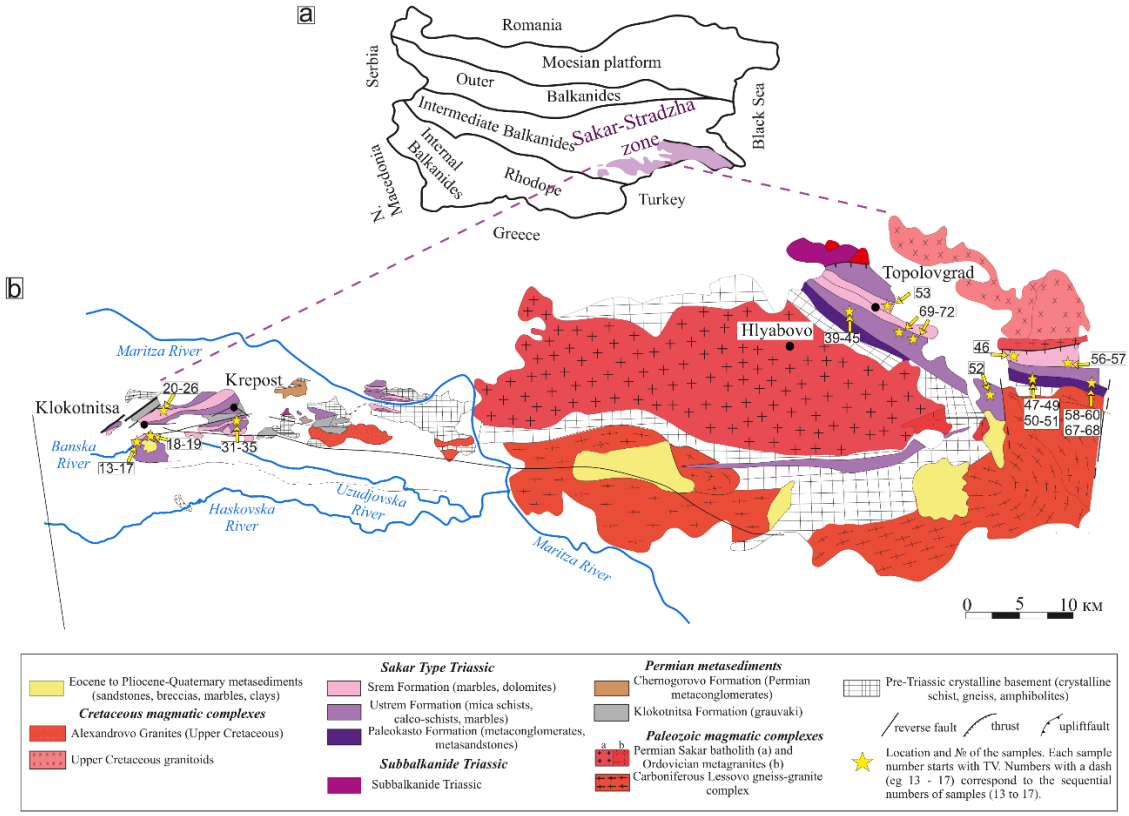

Figure 1. a) Tectonic subdivision of Bulgaria [27]; b) simplified geological map of Sakar unit compiled after [22,28,74].

Triassic metasedimentary complex's protoliths of the Sakar unit (assigned to Sakar-Type Triassic (STT) in east part, [22] consist of basal conglomerates and arkosic sandstones, passing upward into lithic sandstones with pelitic alternation and impure limestones, determining shallow and deep-marine to turbiditic deposition [22,48]. Sediment deposition ends with limestones and solostones, whose metamorphic analogues contain preserved fossils from the Early and Middle Triassic (crinoids, bivalves, conodonts; [53,54]. The metasediments from the westernmost deposits is not

 doi:10.20944/preprints202507.0182.v1

study in detail, but [24] assigned them to the STT as Terrigenous-carbonate Sakar-type Triassic (TCSTT), which could be correlated to the Ustrem Formation. Sr isotopes on carbonate rocks suggest a Late Palaeozoic and/or Mesozoic time of sedimentation [56]. Detrital zircon ages in metasediment cover range from Ordovician (433–446 Ma) to Carboniferous (305 Ma) [34,40,48,57–59] and are consistent with the time of crystallisation of metagranitoids in the basement. Both cover and basement were affected by greenschist to amphibolite facies metamorphism during the Late Jurassic–Early Cretaceous time [34,40,48,57–59] followed by rapid post Late-Jurassic cooling inferred by fission track dating [36].

The geological evolution of the SSZ is related to Variscan/Hercynian orogenesis, produced by a long-lived, Ordovician to Triassic magmatic arc, evolved on the northern side of Palaeo-Tethys [32,39,48,69]. The SSZ represents the continuous accretion of the northern Gondwana margin to Eurasia from the mid-Paleozoic to the Cimmerian. It preserves Precambrian continental blocks, interpreted as remnants of the northern Gondwana margin e.g., [35], and is assigned to the southern passive continental margin of Eurasia [70].

3. Analytical Procedure

Forty-six samples were collected of the Sakar metasedimentary cover for petrographic observations, geochemical studies, and U-Pb zircon geochronology. Table 1 provides a list of the samples with their GPS coordinates. The sampling locations are shown in Figure 1b. The major elements were determined by X-ray Fluorescence (XRF) in Karlsruhe, Germany by Bruker AXS XRF spectrometer and in Bureau Veritas Minerals, Vancouver (Canada). The analysis was performed on powder pellets prepared using an HTP press at a constant pressure of 15 tons for 20 seconds. Loss on ignition was measured using a standard method. For XRF at Bureau Veritas Minerals, Vancouver (Canada), the analysis was performed on Li2B4O7/LiBO2 fusions, using standards STD OREAS184 and STD SY-4(D). The XRF at Sofia University "St. Kliment Ohridski" uses EDXRF Epsilon 3XLE instrument (PANalytical), software–Omnian 3SW. The quantitative analysis was performed in a melt obtained by homogenizing approximately 1 g of sample with added 3 g of lithium metaborate ($LiBO_2$) and 6 g of lithium tetraborate ($Li_2B_4O_7$), used as fluxes. Trace elements were measured by LA-ICP-MS (New Wave Research (NWR) 193 nm excimer laser UP-193FX attached to a Perkin-Elmer ELAN DRC-e quadrupole inductively coupled plasma mass spectrometer) at the Geological Institute, Bulgarian Academy of Science in Sofia, Bulgaria, using SiO_2 and CaO as internal standards and NIST 610 as external standard. Zircon separation of 8 samples followed standard techniques using heavy liquids. The selected grains (200–60 μm) were arranged in epoxy resin and dated by LA-ICP-MS of U-Pb dating at the Geological Institute of BAS, Bulgaria and Magma & Volcans Laboratory in Clermont-Ferrand, France using GJ1 as primary and Plešovice as secondary standard. The used ages are at a 10% level of discordance ($(^{206}Pb/^{238}UMa)/(^{207}Pb/^{235}UMa)$ *100) accompanied by calculation a non-iterative probabilistic model for determining a single concordant age and its concordance class 1 to 7, [71]. Detrital zircons belong to the Ustrem (TV-13, TV-17, TV-39, TV-40, TV-41, TV-45, TV-48) and Paleokastro Formations (TV-49).

4. Field Observation and Sampling

The main outcrops of STT and TCSTT metasediments are to the east and west of the Sakar batholith (Figure 1b). The main outcrops are near Topolovgrad city to the east and Klokotnitza village to the west.

In the eastern part, the metasediments correspond/belong to STT [22]. The lowermost Palaeokastro Formation consists of (metasandstones and metaconglomerates, formed in a continental environment with typical alluvial characteristics [72]. The terrigeneous material is represented by rounded and semi-rounded quartz crystals of ~3 cm in size (Figure 2a), surrounded by a finer-grained matrix of chlorite, biotite, muscovite, and epidote. Fine- to coarse-grained metasandstones contain quartz, white mica, biotite, feldspar, rounded and semi-rounded granite and gneiss fragments

 doi:10.20944/preprints202507.0182.v1

(Figure 2b). The gradually overlying metaclastic-carbonate Lower Triassic Ustrem Formation comprises an uneven alternation of calcite-biotite schist (Figure 2c), quartz-muscovite schist, muscovite-quartz schist and marbles. In sandy marbles, metasandstones and quatz-amphibolites of the Ustrem Formation are preserved bivalve shell negatives (e.g., *Myophoria costata*, *Myalina* spp.) and crinoids [22,72], which indicate Upper Triassic age of sediments. The Ustrem Formation comprises Lower Triassic bivalves in upper levels, conformably overlain by conodont-bearning Middle Triassic calcite and dolomite marbles of the Srem Formation (Figure 2d, [22]). The metasediments of Sakar type Triassic were deposited in a fluvial to shallow marine carbonate platform setting, and for a short period in Early to Middle Triassic, they reached a thickness of over 2400 m [22].

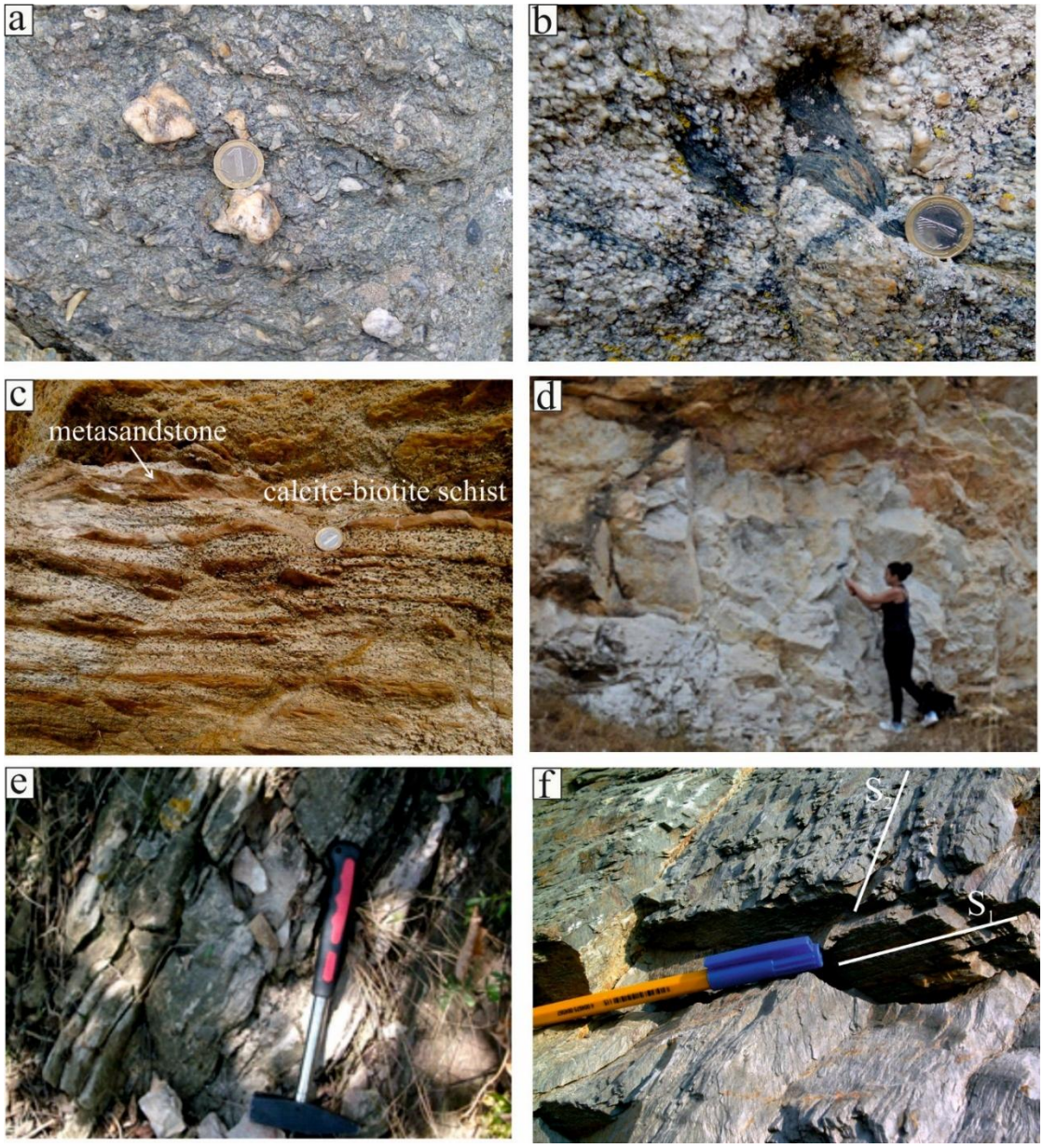

Figure 2. Field photographs of the Triassic metasedimentary sequence: a) large quartz clasts (~3 cm) in metaconglomerate (STT, TV-49); b) metasandstone containing various fragments of gneisses and granites (STT, TV-60; c) alternation of metasandstone (TV-47) and calcite-biotite schist (TV-48) (STT); d) thick-layered to massive porcelain-like marbles (STT, TV-52); e) quartz-muscovite schist composed of alternating quartz and mica bands (TCSTT, TV-13a); f) fine-grained phyllites with two perpendicular foliation planes (TCSTT, TV-24a). The scale bar coin diameter is 2.54 cm.

 doi:10.20944/preprints202507.0182.v1

In the western outcrops in the Klokotnitsa Village area (Figure 1b) Triassic metasediments transgressively overlie Late Palaeozoic terrigenous silicate-carbonate series [73,74]. The lithological sequence starts with metaconglometrates, metasandstones, muscovite-calcite schist, muscovite-dolomite schist, quartz-muscovite schist (Figure 2e) and phyllites (Figure 2f). The upper part of the succession is dominated by carbonate rocks (calcite-, dolomite-, or impure marbles and carbonate-silicate schists). Better visible in marble quarries, the metasediment layers are sub-vertical and folded, often with alternation of silicate- and carbonate-dominated layers. The greenish phyllite, composed primarily of muscovite, quartz, and chlorite, exhibits two distinct foliation planes (Figure 2f), reflecting the complex deformational history of the region.

5. Petrographic Observation

According to the systematic of metacarbonate rocks' modal composition (Rosen et al. 2007), the following lithologies can be distinguished: pure marbles (> 95% carbonate minerals), impure marbles (50–95% carbonate minerals), carbonate-silicate rocks (5–50%), silicate and carbonate-bearing silicate rocks (< 5%).

5.1. Pure Marbles

The structure of pure calcite and dolomite marbles is granoblastic with unclear foliation. The metamorphic recrystallisation leads to the amalgamation of mineral grains and the appearance of deformation lamellae in calcite. The best foliation is traced by elongate calcite grains and muscovite found in the marbles from the area of Oreshnik village (Figure 3a). Bioclasts (crinoid fragments) and fine-grained partly recrystallized fossil remains with irregular to oval shape are common (Figure 3b). The most common silicate minerals are quartz and muscovite. Opaque minerals are abundant in various shapes and sizes, detrital rutile is less frequently observed.

 doi:10.20944/preprints202507.0182.v1

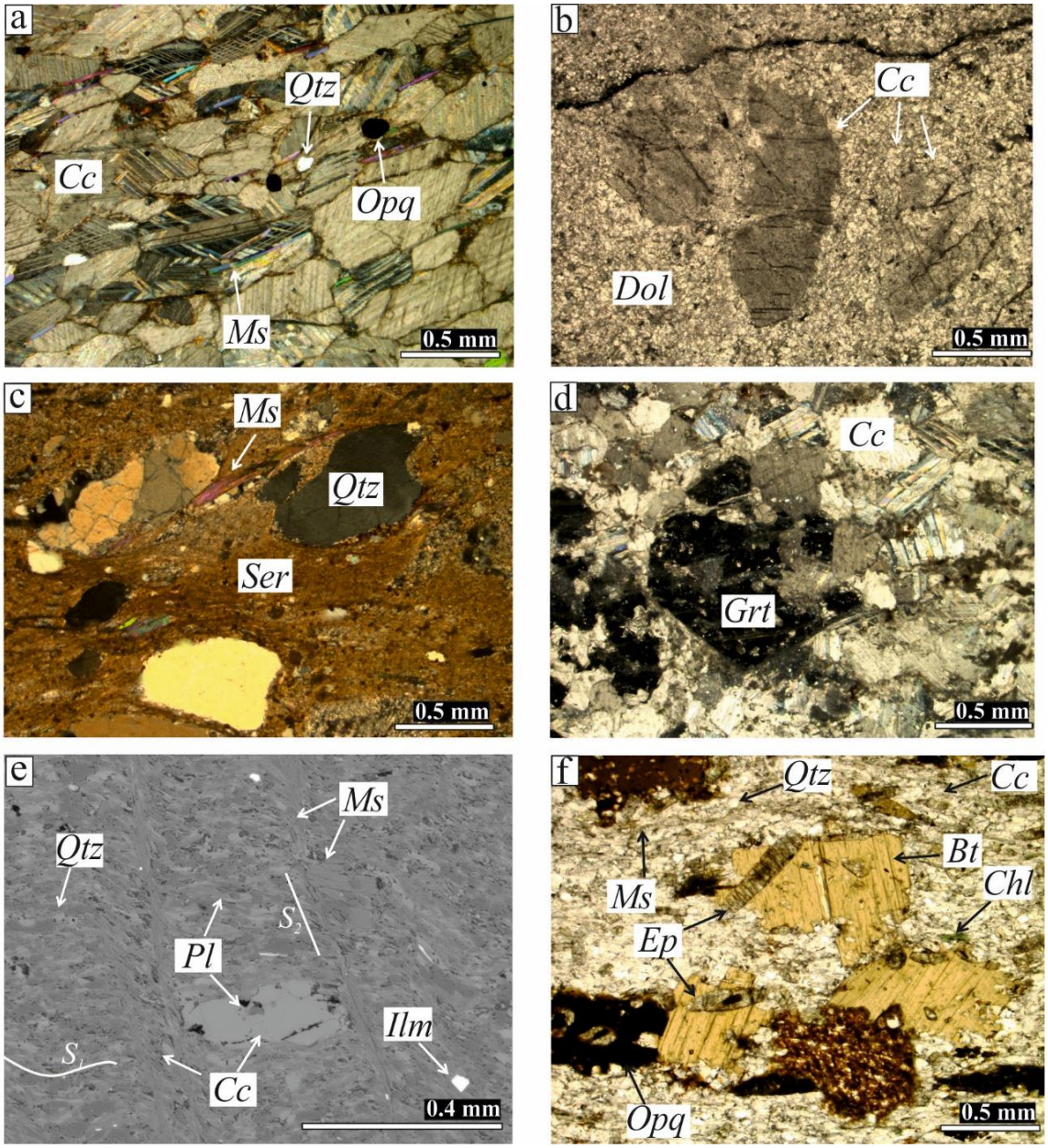

Figure 3. Photomicrographs of selected Triassic carbonate and carbonate-silicate rocks: a) elongate calcite grains and muscovite flakes, that define the foliation in pure calcite marble, single quartz and opaque minerals are also present (XN, TV-70, STT); b) Bioclasts (crinoid fragments) or well-defined areas of oval or arcuate shape in pure dolomite marble (XN, TV-46, STT); c) Quartz clasts in fine-grained sericite-carbonate matrix with relict clay minerals, impure marble (XN, TV-26, TCSTT); d) subhedral grossular-rich garnet in calcite matrix, impure calcite marble (XN, TV-51, STT); e) calcite porphyroblasts in chlorite-muscovite matrix that preserves S_1 and S_2 foliations (BSE, TV-24, TCSTT); f) biotite porphyroblasts with inclusions of quartz and epidote in a fine-grained muscovite-quartz-calcite matrix with larger hematite-magnetite (Opq) clusters, calcite-biotite schist (IIN, TV-48, STT).

5.2. Impure Marbles

The impure marbles are dominated by elongate calcite with deformation twins, and rarely by rhombohedral dolomite grains. Carbonate minerals are present by coarser sub- to euhedreal crystals, and dolomite often forms uniform-grained monomineral areas. The foliation is marked by minor thin phyllosilicate (muscovite, ±chlorite) bands, defining lepido-granoblastic to granoblastic texture. Rhombohedral calcites suggest former dolomite crystals that underwent dedolomitization during metamorphism [75], and associated thin Fe oxide/hydroxide rims point to demixing during this transformation [76].

 doi:10.20944/preprints202507.0182.v1

The well-presented clasts of quartz, plagioclase, and K-feldspar are the common silicate minerals. The mica bands with elongated plagioclase grains are captured by polygonised quartz aggregates. Relict clay mineral component is inferred to be present in the fine-grained matrix of the TCSTT impure marbles (Figure 3c). The impure marbles from the eastern outcrops contain subhedral rich in grossular garnet porphyroblasts (Figure 3d) and in smaller amounts epidote and diopside. Opaque minerals (magnetite, pyrite and hematite) are abundant and oriented along the foliation. Syn- to postmetamorphic coarse-grained calcite veins crosscut the foliation and lead to remobilization and recrystallization of minerals from the finer-grained matrix.

5.3. Carbonate-Silicate Rocks

The foliation of carbonate-silicate rocks (e.g., muscovite-calcite schist, muscovite-dolomite schist, calcite-biotite schist) is traced by phyllosilicate bands alternating with bands of calcite or dolomite with deformation lamellae. Plagioclase grains are often included in phyllosilicate bands, and are parallel to the foliation. Lenticular to recrystallized polygonal quartz aggregates are also distinguished. K-feldspar clasts are rounded with microcline twinning, enveloped by quartz-muscovite pressure shadows and dolomite lenses. The phyllites of TCSTT preserve two perpendicular foliations (S_1–traced by muscovite, chlorite, calcite, ilmenite, quartz; S_2–traced mainly by muscovite) and small synkinematic porphyroblasts of calcite, chlorite, and muscovite subparallel to S_1 foliation (Figure 3e). Carbonate-silicate schists from the eastern outcrops do not contain dolomite and K-feldspar, but syn- to postkinamtic biotite and epidote porphyroblasts and opaque minerals (hematite and magnetite) aggregates form. Bioite porphyroblasts include numerous minerals from the matrix and larger epidote grains (Figure 3f). The growth of biotite porphyroblasts with abundant epidote inclusions marks the increasing temperature, without significant deformation. Syn- to postkinematic porphyroblasts formation is typical phenomena for the area and is accompanied by quartz and calcite annealing. Oxidized calcite clast are resorbed and randomly distributed in the sample.

5.4. Silicate and Carbonate-Bearing Silicate Rocks

The foliation in silicate and carbonate-bearing silicate rocks (muscovite-biotite-quartz schist, muscovite-chlorite schist, garnet-biotite-muscovite schists) is defined by alternation of thin phyllosilicate (muscovite, ±chlorite, ±biotite) bands and quartz-feldspatic bands with intensive static recrystallization (Figure 4a). The metaterrigenous rocks (metasandstones and metaconglomerates of the STT) are characterized by a muscovite–sericite recrystallized matrix, within which large isometric polycrystalline quartz clasts dominate, along with plagioclase, K-feldspar, and occasionally calcite. Both rock types contain phyllosilicate-rich bands with prismatic, elongated plagioclase crystals and euhedral epidote (~0.05 mm), aligned with their long axes parallel to the foliation. Quartz clasts (~1 cm) exhibit undulose extinction. Sericitized K-feldspar clasts show microcline grid patterns and, more rarely, carlsbad twinning. Plagioclase clasts are strongly sericitized and display deformation lamellae. Calcite clasts are xenomorphic and contain numerous inclusions of quartz and, less commonly, chlorite.

In our samples garnet appear as larger, disintegrated clasts, resorbed and replaced by chlorite and biotite (Figure 4b) and with probably detrital origin. In quartz-richer schists, smaller oval-shaped grains grew during the last Mesozoic metamorphic event (Figure 4c). In phyllosicate rich samples the postkinematic garnet porphyroblasts grow (Figure 4d). Syn- to postkinematic porphyroblasts of biotite and epidote (~ 2mm), grow in carbonate-bearing silicate samples (Figure 4e). The postkinetamatic calcite veins are coarser-grained and crosscut the foliation, and exhibit brownish-red Fe oxides and hydroxides along cleavage planes. The association of the newly formed metamorphic minerals depends on the detrital material, that built up the sediments protoliths and consequtively on the components available during metamorphic transformations. The accessory minerals are randomly distributed among the samples and large part of them is of detrital origin. High closure temperature of the zircon, makes it a good for the provenance of the sediment material (Figure 4f).

 doi:10.20944/preprints202507.0182.v1

Other accessory minerals have the potential to reequilibrate and to reset their isotope systems during metamorphism (rutile, monazite, apatite) and could date the late metamorphic event. Opaque minerals (magnetite, ilmenite) trace the foliation, suggesting syn-metamorphic formation.

Petrographic observations of diverse Triassic metasedimentary rocks (carbonates, carbonate-silicates, silicates, and carbonate-bearing silicates) within the Sakar Unit revealed distinct mineral associations for each lithological type (Table 2), confirming their para-sedimentary origin. Detrital components include quartz, with subordinate plagioclase and K-feldspar, as well as accessory minerals such as zircon, monazite, and apatite, all indicative of a predominantly granitic provenance. The marble protoliths are interpreted as calcitic and dolomitic limestones containing variable amounts of detrital silicate material. Metamorphic mineral assemblages reflect heterogeneous metamorphic conditions, ranging from lower to upper greenschist facies in the western part of the unit to lower amphibolite facies in the east.

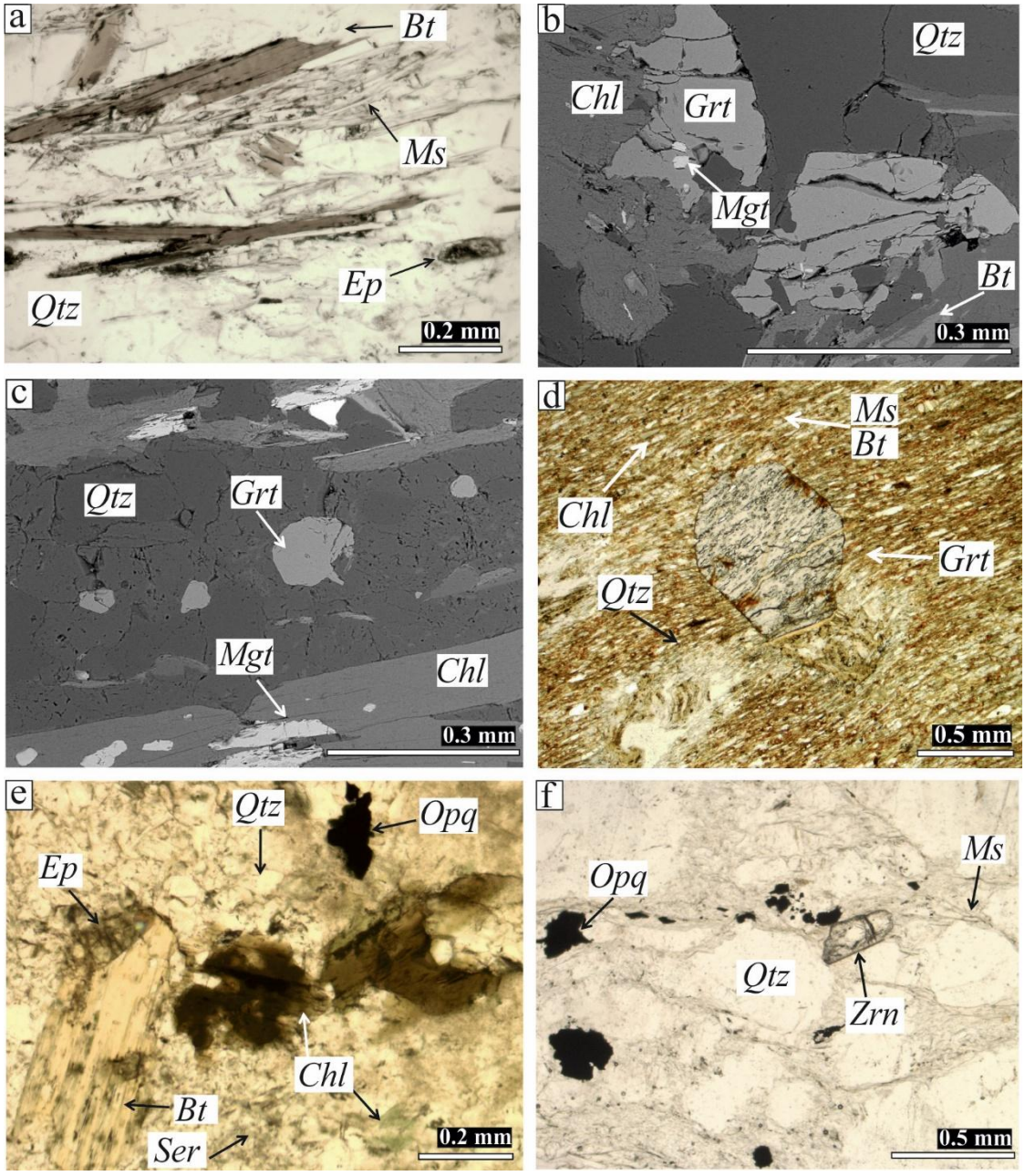

Figure 4. Photomicrographs of selected Triassic silicate and carbonate-bearing silicate rocks: a) biotite-muscovite bands in quartz-dominated matrix, quartz-muscovite schist (IIN, TV-43, STT); b) resorbed and cracked garnet fragments, partially enveloped by chlorite and biotite in muscovite-biotite-quartz schist (BSE, TV-39, STT); c)

 doi:10.20944/preprints202507.0182.v1

smaller, oval garnets that grow during the last metamorphic event, muscovite-biotite-quartz schist (BSE, TV-40, STT); d) postkinematic garnet porphyroblast in a fine-grained matrix dominated by phyllosilicates, garnet-biotite-muscovite schist (IIN, TV-58, STT); e) biotite porphyroblast with epidote inclusions, in chlorite-sericite-quartz matrix, metasandstone (IIN, TV-68, STT); f) zircon and opaque minerals in phyllosilicate bands, metasandstone (IIN, TV-60, STT).

6. Geochemistry

The bulk geochemistry of the metasedimentary rocks is controlled by common carbonate and silicate minerals with detrial or sediment origin. Trace elements contents are controlled mainly by the accessory minerals association, but also by some major minerals.

6.1. Minerals Controlling Whole-Rock Geochemistry

The major oxides in the studied metasedimentary rocks (pure, impure marbles, carbonate-silicate rocks, carbonate-bearing silicate rocks and silicate rocks) are presented in Table 3. The correlation coefficient (r) used is derived from the whole-rock data. The main content of CaO and MgO participates in carbonate minerals (calcite and dolomite), confirmed by a negative correlation between CaO+MgO and SiO_2 (Figure 5a). The pronounced negative relationships between $r(SiO_2, CaO)$ = -0.90 compared to $r(SiO_2, MgO)$ = -0.51 correspond to calcite dominance. Excluding dolomite-bearing rocks, the participation of MgO (< 5 wt%) in silicate minerals (chlorite, biotite) is evidenced by positive correlations with (Figure 5b). A positive and negative trend is distinguished in the correlation of SiO_2 with Al_2O_3, TiO_2, $Fe_2O_3^*$ and K_2O (Figure 5c, d). The positive relationship observed for SiO_2 < 60 wt.% confirms the predominance of chlorite, white mica and feldspar over quartz. Conversely, the negative correlation of SiO_2 (> 60 wt%) with Al_2O_3, TiO_2, Fe_2O_3 and K_2O corresponds to quartz dominance over the other silicate minerals. The positive correlation between Al_2O_3 and K_2O (Figure 5e) is due to the presence of muscovite, biotite and K-feldspar in the mineral composition. The ratio K_2O/Al_2O_3 is most often in the characteristic interval for muscovite (0.2–0.4, [77]), which shows the leading role of this mineral in the distribution of K and Al in the studied samples. The Na_2O/Al_2O_3 ratio (Figure 5f) ranges from values typical of muscovite (≤ 0.02) to plagioclase (≥ 0.40), the main sodium-bearing mineral in these rocks.

 doi:10.20944/preprints202507.0182.v1

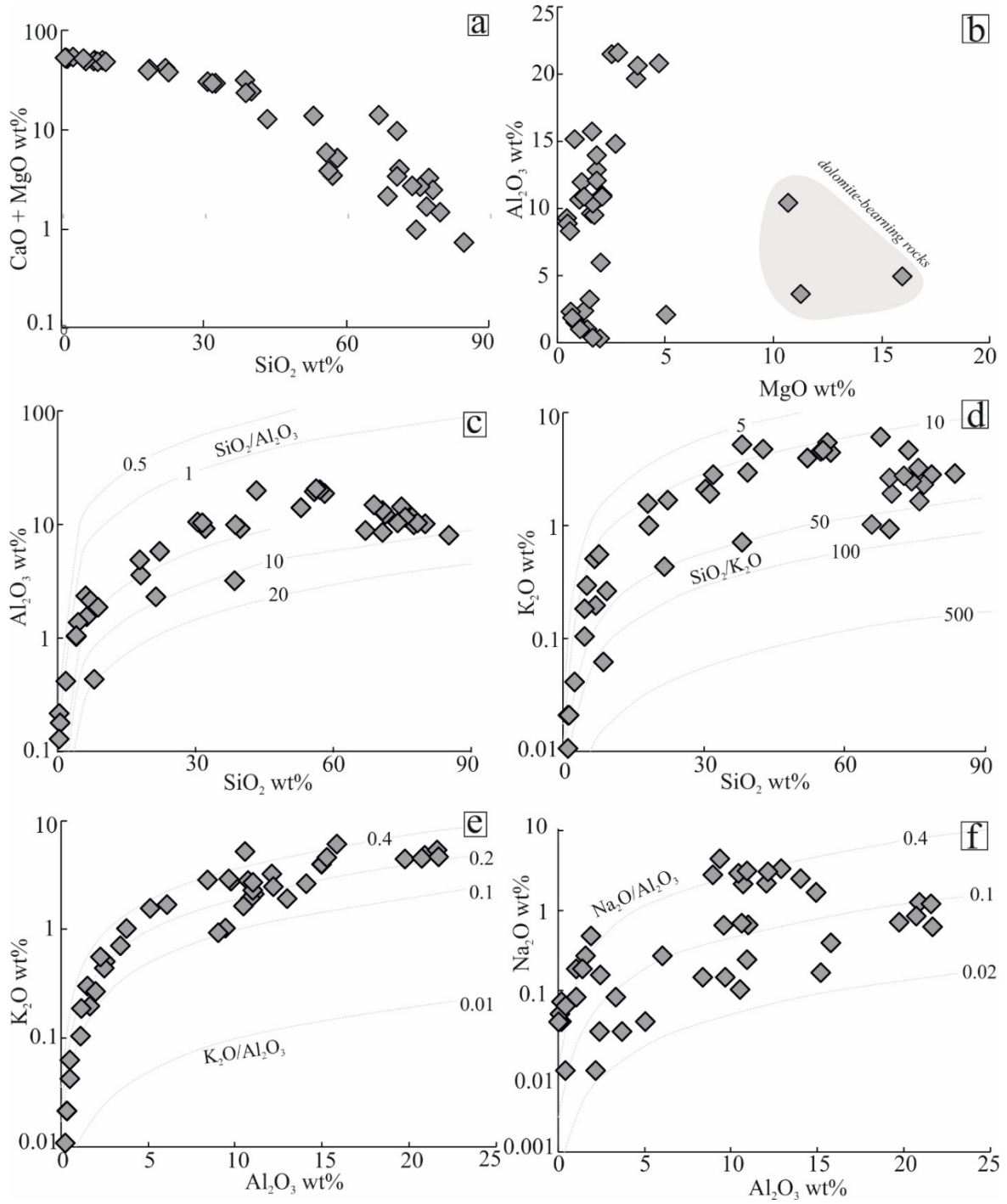

Figure 5. Correlation diagrams of major oxides (wt %): a) SiO_2 vs CaO + MgO negative correlation (r = -0.99); b) MgO vs Al_2O_3; c) SiO_2 vs Al_2O_3 and SiO_2/Al_2O_3 isolines; d) SiO_2 vs K_2O and SiO_2/K_2O isolines; e) positive correlation between Al_2O_3 vs K_2O and K_2O/Al_2O_3 isolines; f) Al_2O_3 vs Na_2O diagram and Na_2O/Al_2O_3 isolines.

6.2. Minerals Controlling the Whole-Rock Trace Elements Composition

The contents of trace elements in bulk rock samples are provided in Table 4 and 5. Most of the trace elements (Sc, Ti, V, Cr, Co, Ni, Cu, Ga, Rb, Y, Zr, Nb, Sn, Sb, Cs, Ba, Hf, Ta, W, Pb, Th, U, REE) are carried by the silicate minerals, confirmed by statistically significant positive correlation with the silicate major oxides and negative correlation with CaO, e.g., $r(Zr, CaO)$ = -0.81. The contents of alkaline and alkaline earth trace elements correlate positively with K_2O $r(Rb, K_2O)$ = 0.87, $r(Cs, K_2O)$ = 0.76, $r(Ba, K_2O)$ = 0.76), which indicates their association with the most common potassic rock-forming minerals (white mica, biotite, K-feldspar, Figure 6a). This is supported by low Rb content (~1 ppm)

 doi:10.20944/preprints202507.0182.v1

in marbles as opposed to the mica abundance samples (e.g., Grt-Bt-Ms schist TV-58 with Rb = 435 ppm). Gallium content reaches up to 64.6 ppm in mica- and chlorite-rich rocks replacing isovalently Al $r(Ga, Al_2O_3)$ = 0.86, Figure 6b) into aluminosilicate minerals (micas, feldspars, epidotes, garnets). The uneven content of $Fe_2O_3^*$ (higher values in terrigenous rocks 0.86–6.47 wt.% and rutile-ilmenite-bearing rocks 1.15–7.59 wt.%) show strong to moderate positive correlations with transition metals (rSc = 0.65, rV = 0.59, rCr = 0.52, rCo = 0.53, rNi = 0.62, rZn = 0.63) indicating residence in mafic (e.g., biotite, chlorite, garnet) and accessory (rutile, ilmenite) minerals.

The high field strength elements HFSE (Zr, Hf, Ta, Nb) and actinide (Th, U) reside in accessory minerals, and rarely in rock-forming minerals by isomorphic substitution of major elements (e.g., Ti). The strong positive correlation between Zr and SiO_2 (at SiO_2 from 0.4 to 60 wt%, Figure 6c) is related to the increased proportion of detrital zircon, mostly other accessory minerals present with increasing silicate component in rocks. The lack of correlation observed at SiO_2 > 60 wt% is associated with the increasing dominance of quartz and a corresponding decrease in zircon, which is corroborated by the consistent Zr/Hf ratio of ~ 40.

The Th and U content and Th/U ratio increase from carbonate to silicate rocks (Figure 6d from 0.28 to 16.47 ppm, mean 4.42) with two trends are observed $r(Th/U, SiO_2<60\ wt\%)$ = 0.81 and $r(Th/U, SiO_2>60\%)$ = 0.68 and correspond to the upper continental crust composition [78]. The Th/U variation could be related to weathering and sedimentation processes, considering the mobilization of oxidized U^{6+} [1,79–81]. Sr is highly abundant in carbonate rocks compared to other elements (Figure 6e). Its preference for calcite is confirmed by higher Sr contents (220–4268 ppm) in calcite marbles and lower contents (58–195 ppm) in dolomite and calcite-dolomite marbles (Figure 6f). Higher Th/U ratio (0.28–7.33) and uranium contents (0.24–4.18 ppm) in metacarbonate rocks point to oxic environment of precipitation.

 doi:10.20944/preprints202507.0182.v1

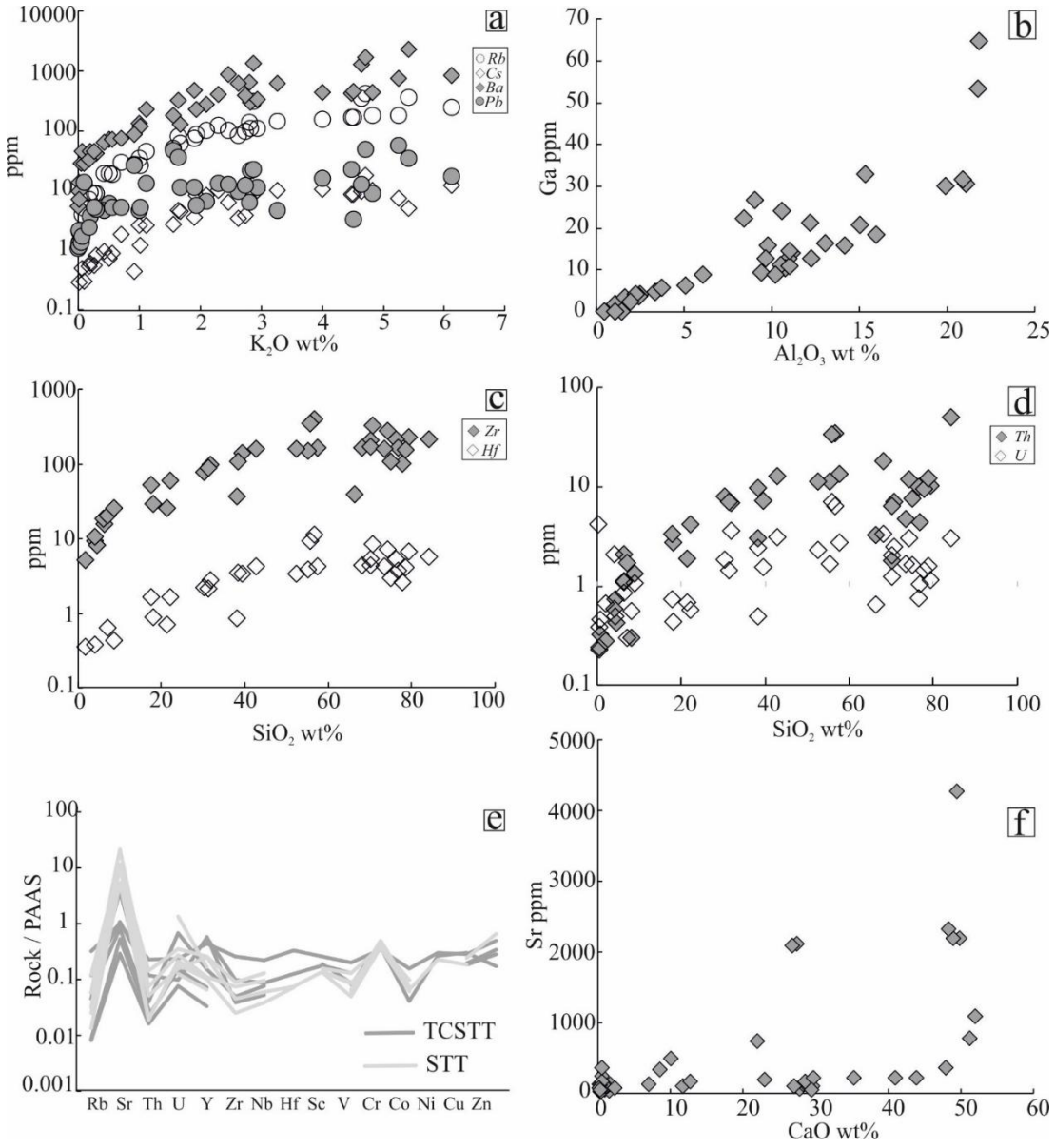

Figure 6. Geochemistry of selected trace elements: a) positive correlation K_2O wt% vs. Rb, Cs, Ba and Pb ppm; b) positive correlation Al_2O_3 wt% vs. Ga ppm; c) SiO_2 wt% vs. Zr and Hf ppm; d) correlation between SiO_2 vs. Th and U ppm; e) PAAS-normalized spider diagram for trace elements (values of [82]; f) correlation between CaO wt% and Sr ppm.

The contents of rare-earth elements (REE) are presented in Table 4. The PAAS values and chondrite [78,82] are used for normalization of metacarbonate and metasiliciclastic rocks, respectively. Most of the HREE in metacarbonate rocks were under their detection limits, but the few REE-Y patterns are like see water REE pattern: with LREE depletion (average $(Nd/Yb)_n$ = 0.51, n=6), negative to small positive Ce/Ce* anomaly (0.39–1.07, average = 0.8, n=12) and positive La anomaly. Ce and La anomalies are sensitive to detrital contamination and in the studied samples indicate precipitation from sea water with some clastic input. The variable detrital input is visible in the lack of positive Eu/Eu* anomaly (0.95-1.61, average=1.21, n=4) [83 and reference therein].

The chondrite-normalized REE diagrams of carbonate-silicate to silicate rocks display LREE enrichment, a flat heavy HREE pattern and a negative Eu anomaly (Figure 7a), equivalent to upper continental crust. The La_N/Sm_N (1.10–4.70) and Gd_N/Yb_N (1.06–2.12) ratios fall into a narrow range for silicate-rich rocks. The prominent Eu depletion (Eu/Eu*= 0.49–0.86, and single Eu/Eu* = 1.01 for metasandstone TV-47) could be related to chemical fractionation within the continental crust, related

 doi:10.20944/preprints202507.0182.v1

to the production of K-rich granitic rocks provenance which typically possess negative Eu anomalies (Figure 7a, [84]).

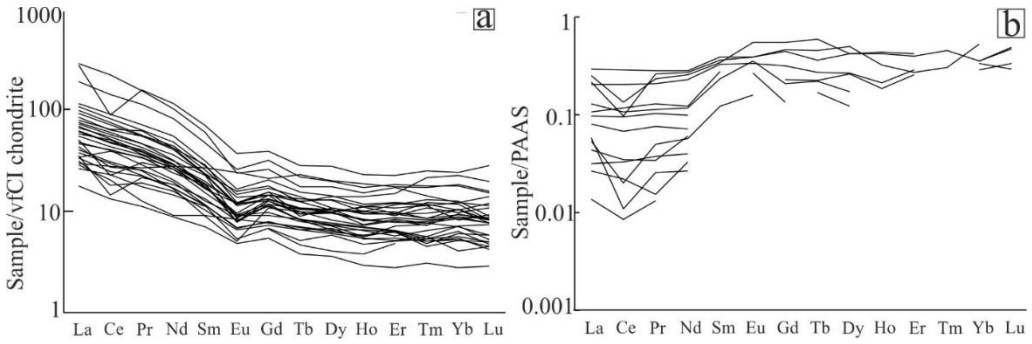

Figure 7. REE patterns: a) chondrite-normalized REE plot of carbonate-silicacate to silicate samples, chondrite values from McLennan (1989); b) PASS-normalized REE diagram of metacorbonates, PAAS values from [78].

6.3. Protoliths: Provenance, Weathering and Hydraulic Sorting

The affinity of most major and trace elements to the siliciclastic component and the low mobility during diagenesis and metamorphism support their use as classification parameters of protoliths and provenance. The geochemical signature demonstrates differences in silicate protolith components such as arkoses, litharenites and graywackes according to the classification diagram of Pettijohn (1972) with low Na_2O/K_2O and SiO_2/Al_2O_3 ratios for clay-rich materials; high Na_2O/K_2O and SiO_2/Al_2O_3 ratios for sandy material (Figure 8a). Some very low values of these ratios, $\log(Na_2O/K_2O) <–1$ and $\log(SiO_2/Al_2O_3) < 1$, appear outside the diagram fields, due to Na mobility during weathering of the source area. The discriminant functions of major oxides recognising the sedimentary origin (Roser and Korsch, 1988) determine quartz dominant province with partial felsic igneous source (Figure 8b). The provenance is primarily characterised as having a dominant acidic to mixed arc source, indicated by La/Th < 5 and Hf < 5 ppm; a minor contribution from an andesitic arc source, where La/Th > 5 while Hf < 5 ppm; and a presence of old sedimentary material with La/Th < 5 and Hf > 5 ppm (Figure 8c, after [78]).

Th/Sc and Zr/Sc ratios are consistent with the upper continental crust composition along with significant sediment recycling, heavy minerals enrichment, particularly zircon (Figure 8d, after [1]). The low mobility elements (La, Sc, Ti, Zr) unambiguously plot in the continental island arc field [2] with slight a slight deviation from the continental island arc field towards the active and/or passive continental margin field (Figure 8e, f).

 doi:10.20944/preprints202507.0182.v1

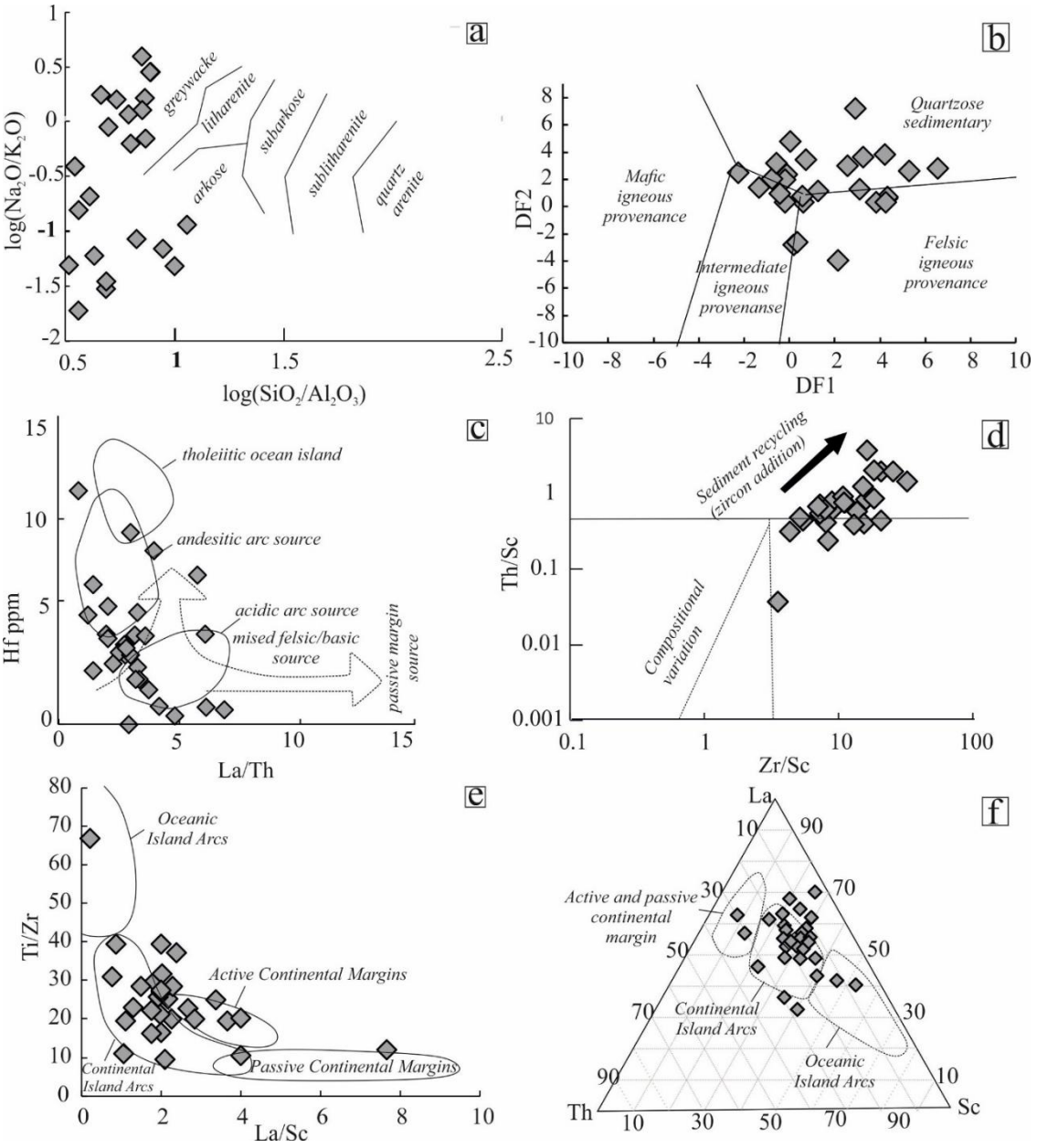

Figure 8. Classification and discrimination geochemical plots: a) diagram of [93]; b) discriminant diagram for province [3], DF1 = (−1.773 TiO2 + 0.607 Al2O3 + 0.76 Fe2O3t − 1.5 MgO + 0.616 CaO 0.509 Na2O − 1.224 K2O) − 9.09; DF2 = (0.445 TiO2 + 0.07 Al2O3 − 0.25 Fe2O3t − 1.142 MgO + 0.438 CaO + 1.475 Na2O + 1.426 K2O) − 6.861; c) La/Th and Hf diagram to determine a sedimentary source [78]; d) Zr/Sc versus Th/Sc plot to determine the degree of sediment sorting [1]; e) Ti/Zr-La/Sc diagram to determine geodynamic setting [2]; f) La-Th-Sc discriminant triangle diagram for determining sedimentary tectonic setting [2].

7. U-Pb Detrital Zircon Geochronology

The U-Pb ages vary from Precambrian to Palaeozoic based on 168 zircon grains, 293 analytical points and 280 concordant results (Table 6). The abundance of data necessitates presenting selected representative data that encompass all age determinations from each sample, given in Table 7, 8 and 9. The major age clusters include Palaeozoic or Palaeozoic to Neoproterozoic zircons with secondary, Meso- and Paleoproterozoic to Neoarchean ages. The key range under 800 Ma features three frequency peaks at 320 Ma, 455 Ma, and 580 Ma, which are linked to variations in source provinces (see Figure 9) with prevalence of Late Ordovician ages in the TCSTT and Carboniferous-Neoproterozoic ages in the STT.

 doi:10.20944/preprints202507.0182.v1

The Late Palaeozoic zircon population (quartz-muscovite schist TV-45, calcite-biotite schist TV-48 and metaconglomerate TV-49) of STT is composed of euhedral, long to short prismatic and minor well-rounded grains, colourless or yellowish to pink. The internal texture is typical for igneous zircon with euhedral homogeneous core and oscillatory-zoned rims (Figure 10a-k) or fully oscillatory zoned grains (Figure 10l). The grains with completely homogeneous (Figure 10m, n, o), complex and weak convolute zoning (Figure 10p, q) or with occasionally thin recrystallised rims are rare. The age variation (287–622 Ma) yielded an Early Permian–Late Carboniferous cluster (287–346 Ma) and a second group of Early Silurian–Neoproterozoic ages (439–622 Ma). The younger ages are related to concentric zoning, homogeneous cores and completely zoned grains (Th/U = 0.13–1.49). The Th/U ratio (0.09–0.94) in oscillatory or homogeneous zones where the older ages were measured is comparable and suggests a magmatic origin consistent with the internal zircon texture. The sample TV-45 (coarse-grained fraction) demonstrates Early Permian-Late Cambrian variety (305-501 Ma) with Carboniferous predominance (305–346 Ma, Th/U = 0.13–1.11) and major age cluster of ~ 330 Ma (Figure 10r, s). The youngest zircon age is 305.1 ± 4.3 Ma (№ 3c, Table 7). The zircon ages from TV-48 sample vary between 287 and 586 Ma with maximum frequency at ~300 Ma (Figure 10t, u) and Th/U = 0.26–1.49. The data defines the earlies time of zircon input during Early Permian. The results < 300 Ma (286.5–298.2 Ma in 5 zircon grains (№ 9-c, 11-c, 13-c, 13-r, 15-c, 17-r, Table 7) yield concordant age of 297.0 ± 2.4 Ma (MSWD of 0.98, Figure 10v) and preserved primary morphology of close source provenance. The zircon ages in sample TV-49 scatter from Early Permian to Neoprotezoic (307–622 Ma) with major group from 300 to 350 Ma. The coarse-grain zircons show older ages (330–622 Ma, cluster at 333 Ma) compared to younger ages in fine-grain grains (307–345 Ma, cluster at 320 Ma, Figure 10w). A single crystal from the fine-grained fraction (№ 36, Table 7) yielded the youngest ages in this study. The euhedral core and oscillatory-zoned rim display youngest ages of 310.1 ± 3.8 Ma and 307.1 ± 3.7, respectively (№ 36, Table 7) with concordant age of 308.1 ± 2.5 Ma with a MSWD of 1.3 (not shown) and defines Late Carboniferous maximum age deposition.

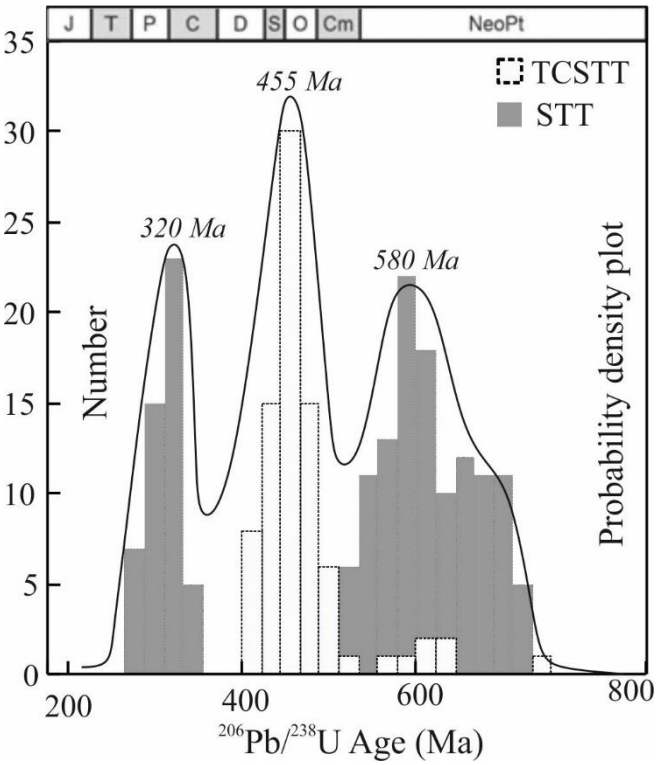

Figure 9. Probability density plot for the most common U-Pb ages of the studied detrital zircon.

 doi:10.20944/preprints202507.0182.v1

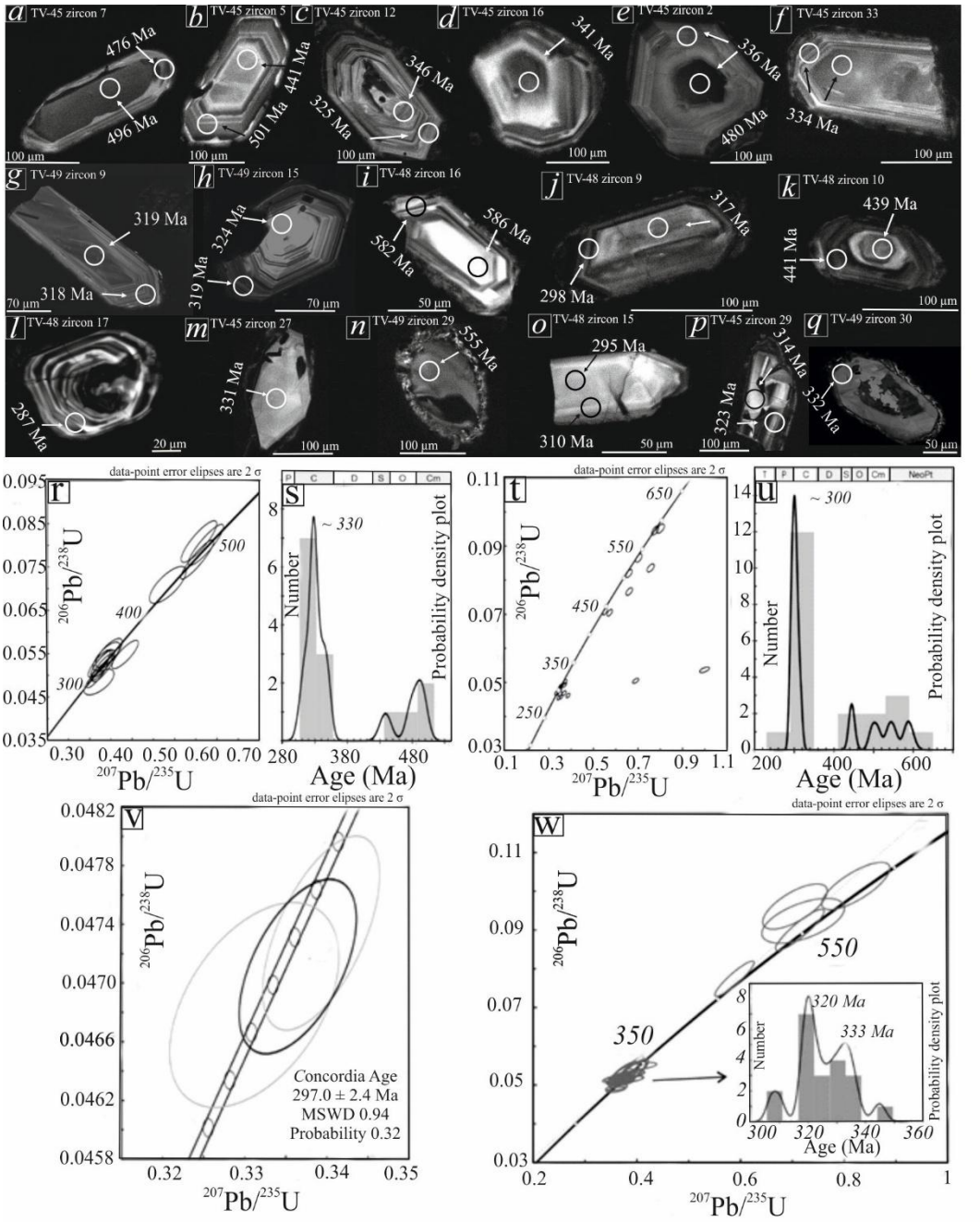

Figure 10. CL images of zircons (60-200 µm) and U-Pb detrital zircon geochronological data from quartz-muscovite schist (TV-45), metaconglomerate (TV-49) and calcite-biotite schist (TV-48) of STT. White circles correspond to $^{206}Pb/^{238}U$ ages. The grains are assigned to sample and zircon number Table 7. a-k) concentrically zoned zircons with homogeneous cores with oscillatory rims; l) entirely oscillatory zonation; m), n), o) homogeneously zoned; p) and q) complex zoned; r, s) concordia diagram with major age group and probabilitity density plot (TV-45); t, u) concordia diagram with major age group inset (TV-48); v) concordia diagram with major age group inset (TV-49); w) concordia diagram of youngest group age 297,0 ± 2,4 Ma, MSWD 0,98 (TV-48).

The Early Palaeozoic, igneous zircons population (quartz-muscovite schists TV-13 and TV-17) of TCSTT comprises colourless, pale to deep pink grains, dominated by subrounded grains with low proportions of euhedral prismatic and completely rounded shapes. The fine-grained zircons (60–100 µm) differs by predominance of long prismatic crystals. The CL images reveal three types of internal structures: 1) xenocrystic cores and osscilatory rims (Figure 11a, b); 2) concentric zoned grains with unzoned euhedral cores and osscilatory rims (Figure 11c, d); and 3) complex textured grains of

 doi:10.20944/preprints202507.0182.v1

recrystallised or newly grown convolute zones (Figure 11e-j). The zircon ages in coarse-grained crystals (200–100 μm, TV-13) vary between ~ 400 Ma and ~1400 Ma, with a major cluster of 460 and several older grains of sub-concordant to discordant ages (580 to 707 Ma and 903 to 1430 Ma, Figure 11k, l). Euhedral cores range from 405 to 481 Ma with an average Th/U ratio of 0.27; the age range for the oscillatory zones is 440 to 473 Ma with an average Th/U of 0.25; for grains with complex to convolute zoning, the ages range from 410 to 461 Ma with an average Th/U ratio of 0.20. In fine-grained zircon fraction (100–60 μm, TV-13 and TV-17) the ages range from 406 to 590 Ma with major frequency ~ 420 Ma (TV-13) and ~ 480 Ma (TV-17) (Figure 11k-m) and Th/U ratios 0.14–0.94. Patchy recrystallisation and magmatic zoning disturbances are rarely related with lower Th/U ratios from 0.03 to 0.09, (473–411 Ma, TV-13). The youngest ages (405–412 Ma) were found in 5 grains from both size fractions (TV-13) and they define a concordant age of 404.6 ± 4.9 Ma (Figure 11n) and Early Devonian maximum sedimentation age of the protolith.

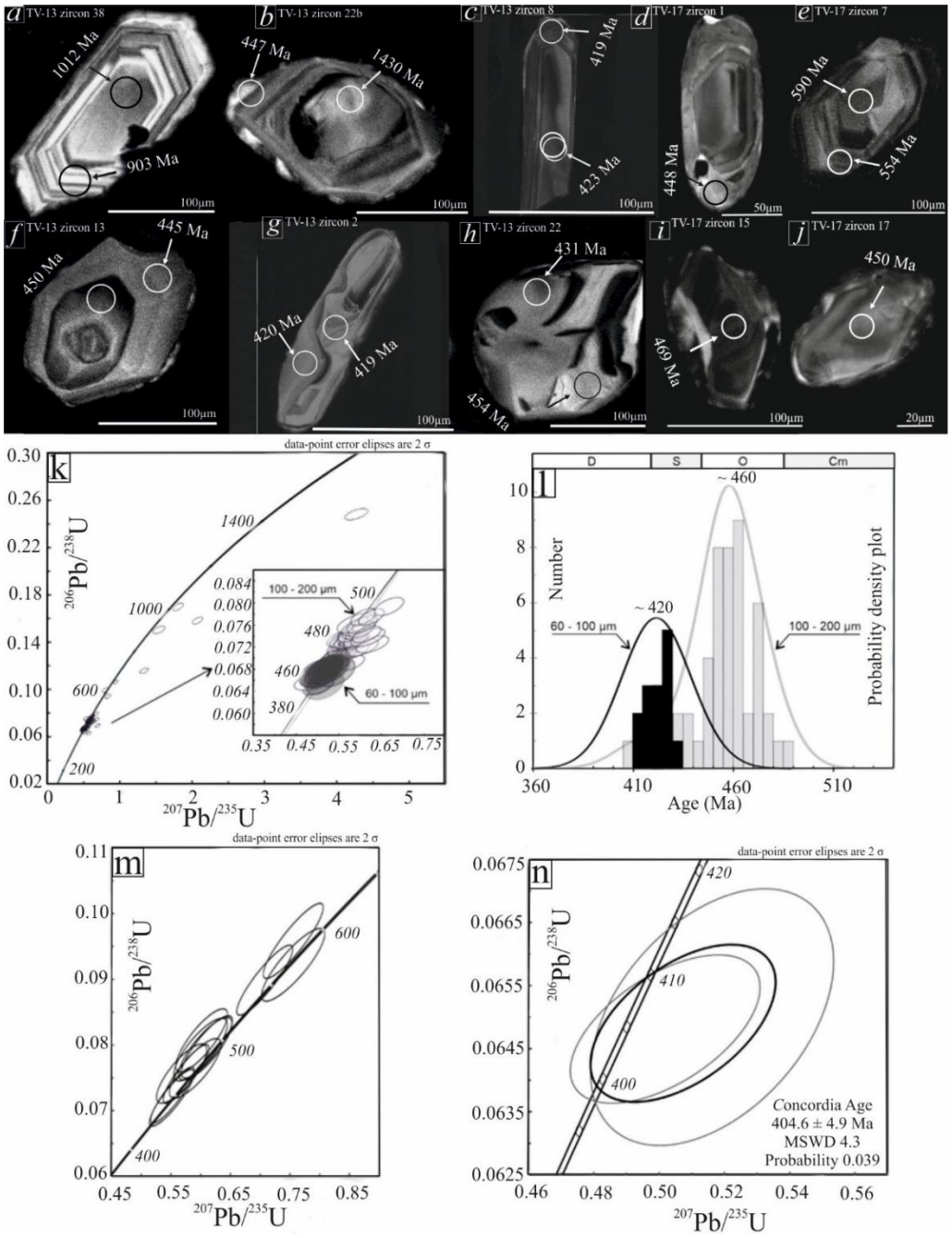

Figure 11. CL images of zircons (60-200 μm) and U-Pb detrital zircon geochronological data from quartz-muscovite schists (TV-13 and TV-17). White circles correspond to $^{206}Pb/^{238}U$ ages. The grains are assigned to

 doi:10.20944/preprints202507.0182.v1

sample and zircon number Table 8. a-f) concentrically zoned zircons with homogeneous cores with oscillatory rims; g), h), i) complex textured grains of recrystallized or newly grown convolute zones; j) homogeneous zircon; k) concordia diagram with major age group inset (TV-13); l) probability density plot of both size fractions (TV-13); m) concordia diagram of all ages (TV-17) n) concordia diagram for youngest zircon 404.6 ± 4.9 Ma (TV-13).

Cambrian and Precambrian ages (Paleoproterozoic to Neoarchean) were obtained for detrital zircons from muscovite-quartz schist (TV-39) and muscovite-quartz schists (TV-40, TV-41) of STT. The zircon grains are semi-rounded, short-prismatic or completely rounded. The dominant internal textures show homogeneous cores with oscillatory-zoned rims (Figure 12a-e), xenocryst cores with homogeneous or oscillatory rims (Figure 12f-j) and completely homogeneous grains (Figure 12k-m). The sectoral zonation (Figure 12n) and complex to convolute structure (Figure 12o) are rarely observed. The age data range from 498 to 2876 Ma with two major clusters: Neoarchaean-Paleoproterozoic and Neoproterozoic-Cambrian. Neoarchean (2545–2876 Ma) and Paleoproterozoic (1731–2385 Ma) ages were established in 14 grains (TV-39, TV-40 and TV-41). These older ages are generally related to xenocryst cores with younger Neoproterozoic and Cambrian mantles, with Th/U (0.09–1.40) ratio indicating magmatic origin. Sample TV-39 exhibits Neoproterozoic-Cambrian ages (Figure 12p), expressed in two major clusters, ~620 and ~530, respectively (Figure 12q). The Neoproterozoic age variation (552–673 Ma with Th/U = 0.12–0.82, except for grain № 11c with 858 and 899 Ma, Table 9) is related to coarse-grain fraction. The fine-grain zircons are distinguished by younger Neoproterozoic ages (548–609 Ma, Th/U = 0.12–0.47) with the presence of Cambrian ages (498–534 Ma, Th/U = 0.11–0.29, Figure 12p, q). The younger (498.2 ± 5.3 Ma) and concordant ages (505.7 ± 7.6 Ma with MSWD 6.3, Figure 12s) can be considered as the earliest time of deposition of the detrital zircon in the sedimentary protolith. The Neoproterozoic age of TV-40 show variation from 543 to 707 Ma (Table 8), with major cluster between 570 and 580 Ma (not shown). The Th/U ratios (0.10–0.94) display magmatic origin. The Cambrian youngest zircon (536.3 ± 6.8 Ma) accepts Proterozoic–Early Cambrian for the earliest time of zircon deposition. The major age of the coarse-grained fraction (TV-41) determine Neoproterozoic age variation from 539 to 937 Ma, with maximum of ~660 Ma and ~550 Ma (Figure 12r). The Th/U ratios from 0.13 to 2.17 indicate predominantly magmatic origin of the detrital zircons, with once expection of low Th/U ratio (Th/U = 0.04, № 15-r, Table 8). The youngest (539 ± 26 Ma, № 12-r, 36-r, Table 9) and concordant ages of 544 ± 15, MSWD = 1.12 indicate Early Cambrian deposition.

 doi:10.20944/preprints202507.0182.v1

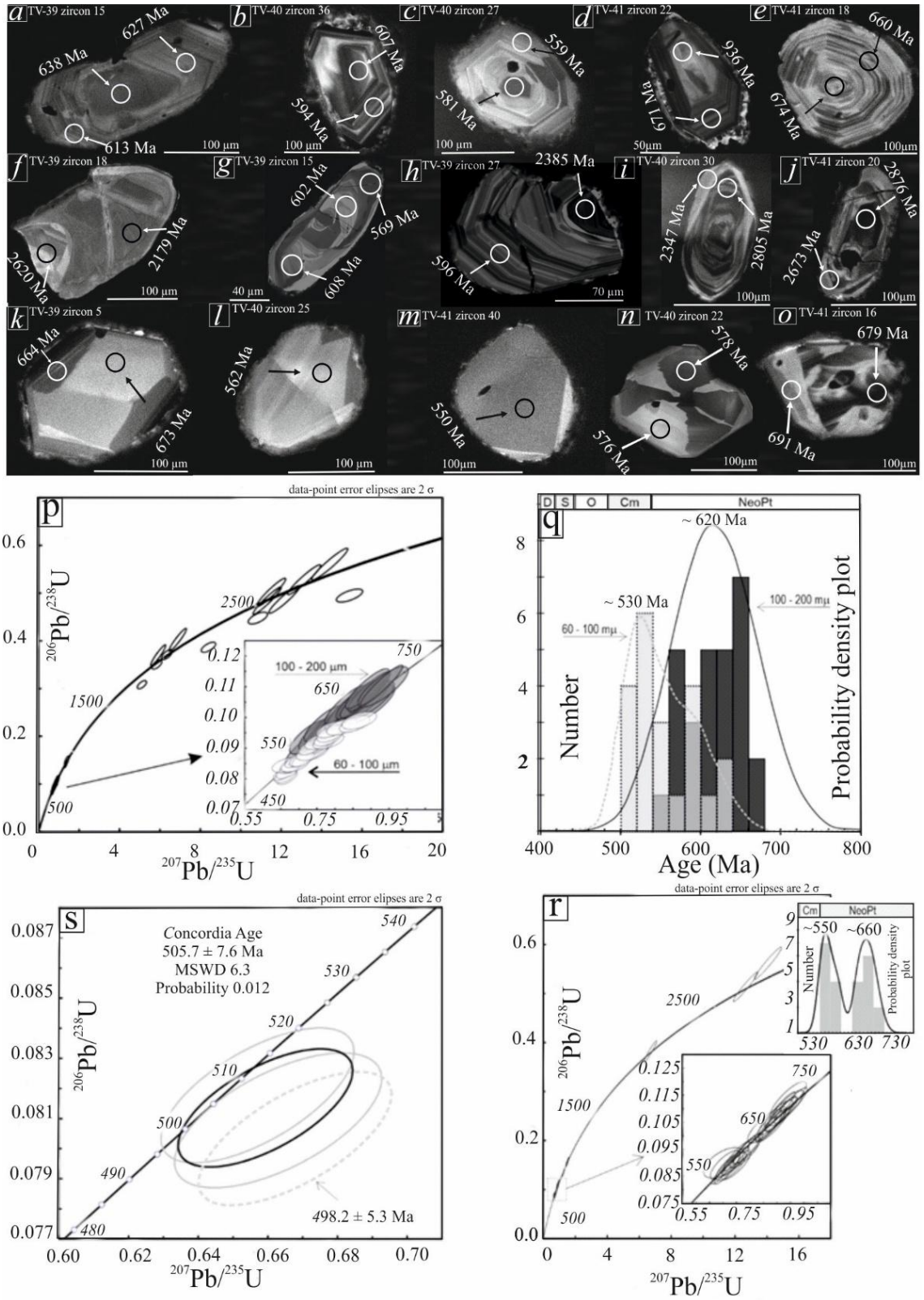

Figure 12. CL images of zircons (60-200 µm) and U-Pb detrital zircon geochronological data from muscovite-quartz schist (TV-39) and muscovite-quartz schists (TV-40, TV-41). White circles correspond to $^{206}Pb/^{238}U$ ages. The grains are assigned to sample and zircon number Table 9. a-e) concentrically zoned zircons with homogeneous cores with oscillatory rims; f-j) xecocrystalline cores with homogeneous or oscillatory rims; k-m) homogeneously zoned; n), o) sectoral to convolute zoned; p) concordia diagram with major age group inset (TV-39); q) probability density plot of both size fractions (TV-39); r) youngest zircons–concordia diagram for 505.7 ± 7.6 Ma included youngest age of 498.2 ± 5.3 Ma–dashed ellipse, (TV-39); r) concordia diagram with major age

 doi:10.20944/preprints202507.0182.v1

group inset from 539 to 692 Ma and probability density plot for all results and inset for most common ages (TV-41).

8. Discussion

The metasedimentary succession in the STT (Topolovgrad area, [22]) correlates with similar TCSTT formations (Klokotnitsa area, [24]). Despite lithology similarities and post-Triassic metamorphism, the metasediments exhibit differences in metamorphic grade with analogous alternation of carbonate-silicate schists, mica schists, and impure marbles, suggesting a comparable protolith composition and depositional setting. However, while the TCSTT is dominated by impure marbles, the STT displays a wider variety of rock types and contains distinctive biotite and garnet porphyroblasts. These mineralogical differences reflect varying degrees of metamorphism. The observed metamorphic minerals indicate low-greenschist facies conditions in the TCSTT [77,79], which increase to low amphibolite facies in the STT [23,25,29,64,77,80–82].

Protolith interpretations of the studied metasedimentary sequence are based on petrographic observations and bulk rock geochemistry. Both suggest protolithic sedimentary rocks composed of quartz, clay minerals, and carbonate minerals, such as arkosic sandstones, shales and limestones. This is supported by the abundant presence of white mica, clastic grains (quartz, K-feldspar, and plagioclase), and calcite. Similar protolith compositions are confirmed by the major oxide contents, which correspond to a previous mixed succession of sandy with high Na_2O/K_2O, SiO_2/Al_2O_3; low Na_2O/K_2O and SiO_2/Al_2O_3 ratios for clay-rich materials and carbonate sediments. The major oxide contents and their correlation coefficients reflect the predominance of quartz over other silicate minerals (chlorite, white mica and feldspar) in the TCSTT and the opposite relationship (predominance of them over quartz) in the STT. The bulk of trace elements (Rb, Ba, Cs, Pb, Zr, Hf, Nb, Ta, Th, U, Ga, Sc, Th, U, Co, Ni, REEs, etc.) is hosted in silicate minerals, with the exception of Sr, which is associated with the carbonate component.

The clastic material in the rocks can be linked to a quartz-dominated provenance with minor contribution from intermediate magmatic sources [3]. Such a source province is typically associated with acidic magmatic bodies that are the source of quartz, K-feldspar grains, and accessory minerals such as zircon. The presence of the latter is confirmed by the high degree of sorting of the sedimentary material with Th/Sc ~ 1 and Zr/Sc > 1. The acidic composition of the source province is further supported by the contents of immobile elements (La, Th, Hf), which indicate a dominant felsic arc source for both studied areas. Discrimination diagrams [2,78] for determining the tectonic setting indicate a dominance of a continental arc setting for the source province. The association of the metasediments with the upper continental crust is also supported by chondrite-normalized REE patterns and the prevailing Th/U ≈ 4 ratio for both study areas. The REE distribution is characterized by higher contents of light REEs, a uniform distribution of heavy REEs, and a negative Eu anomaly. The Europium anomaly may be controlled by the composition of the source province and is commonly associated with granitic rocks [84]. This aligns with models proposing an active continental margin where the subduction of oceanic crust beneath a continental plate leads to the generation of a magmatic arc and concomitant sedimentation in adjacent basins. Observation is directly linked to the Late Paleozoic geological setting related to closure of the Paleotethys Ocean and the formation of an extensive continental island-arc system along the southern margin of Laurussia e.g., [28,51,56,83]. Magmatic processes associated with subduction in this environment generated acidic igneous rocks, which were subsequently eroded and contributed to the composition of the investigated metasediments. Despite ongoing debates regarding the temporal relationship between magmatism and tectonic phases [28,39,41,44,46,52], our geochemical data support a scenario where the erosion of igneous rocks related to subduction processes significantly contributed to the composition of the studied metasediments. It is also plausible that post-orogenic magmatism and sedimentation associated with the collapse and erosion of the Variscan orogenic structure [84] played a role, particularly given the mention of acidic volcanism and supracrustal clastic sedimentation preceding marine sedimentation.

 doi:10.20944/preprints202507.0182.v1

The source rocks of the marbles correspond to limestones with varying proportions of detrital silicate minerals. Trace element contents indicate deposition of the carbonate protoliths in an oxygenated environment, as evidenced by the low U content. Similar interpretations of the protoliths for the Topolovgrad region are consistent with those of [22,85–87]. The negative Ce anomaly is more common in the TCSTT and less common in the STT, often coinciding with the predominance of the carbonate component in the rocks. This suggests its inheritance from seawater. This relationship is supported by the preservation of the primary REE composition of the metacarbonates with a pronounced negative Ce anomaly.

U-Pb geochronology of detrital zircons provides information on the age of deposition of the metasedimentary sequence, which shows some difference in the province of origin of the sedimentary material: a predominance of Early Paleozoic ages (400–500 Ma) in the TCSTT and Cambrian–Neoproterozoic ages (500–700 Ma) in the STT. Internal structures and Th/U ratios indicate a dominant contribution of magmatic zircons with a well-defined maximum in Carboniferous ages, complemented by the youngest data in the Early Permian. Detrital zircons from the STT are associated with Carboniferous-Permian magmatic rocks (346–286 Ma). Abundant information on granites and metagranites with late Carboniferous-Triassic ages in the basement of the studied metasedimentary rocks [28,37,44,46,50] provides an explanation for the nearby sources of magmatic detrital zircons. The potential source can be linked to the established Early Palaeozoic magmatic bodies in the basement of the western part of the Sakar Unit (530.4 ± 6.3 Ma, [40]) and the basement of the eastern part of the Sakar Unit (461.6 ± 2.7 Ma and 489.9-496.7 Ma, [28]). Other possible sources with similar age determinations are magmatic bodies from the Thracian lithotectonic unit (Pervents complex, 452 ± 16 Ma and ~ 470 Ma, [88]) and the basement of the Central Srednogorie (460-500 Ma, [89,90] and 616.9±9.5, 595±23 Ma [91]). Analogous Early Cambrian ages of orthometamorphic rocks are also known in the Strandzha basement (Çatalca, İhsaniye, Binkiliç metagranites) in Turkey (discussion in [92]). This determines the basement of the metasediments as the main source of partially recycled Early Palaeozoic, Cambrian-Neoproterozoic, and older zircons.

9. Conclusions

The TCSTT and STT petrography and whole-rock geochemistry suggest previous sandy, clay and calcareous sediment protoliths. The clastic material is dominantly derived from quartzose sedimentary province with a low proportion of felsic igneous source, deposited into a continental island-arc setting. The petrology observation suggests TCSTT low-grade metamorphism (greenschist facies) increases eastward to STT low-temperature amphibolite facies. U-Pb geochronology of detrital zircons reveals a dominant Carboniferous age, supplemented by early Permian ages, consistent with the presence of Carboniferous-Permian magmatic rocks in the basement. The source province is interpreted as a continental arc, supported by immobile element contents and tectonic setting discrimination diagrams. REE patterns exhibit a negative Eu anomaly, likely inherited from the granitic source rocks. The presence of Early Palaeozoic and Cambrian-Neoproterozoic zircons in the detrital zircon spectra suggests the basement of the Sakar Unit, as well as other nearby units such as the Thracian and Central Srednogorie, as potential sources for the sedimentary material.

References

1. McLennan, S.M.; Hemming, S.; McDaniel, D.K.; Hanson, G.N. Geochemical approaches to sedimentation, provenance, and tectonics. In: Johnnson, M.J., Basu, A., (eds) Processes controlling the composition of clastic sediments, Geol. Soc. Am. 1993, Special Paper 284, London, 21–40.
2. Bhatia, M.R.; Crook, K.A.W. Trace element characteristics of graywackes and tectonic setting discrimination of sedimentary basins. *Contrib. Miner. Pet.* **1986**, *92*, 181–193, https://doi.org/10.1007/bf00375292.

 doi:10.20944/preprints202507.0182.v1

3. Roser, B.; Korsch, R. Provenance signatures of sandstone-mudstone suites determined using discriminant function analysis of major-element data. *Chem. Geol.* **1988**, *67*, 119–139, https://doi.org/10.1016/0009-2541(88)90010-1.
4. Feenestra, A.; Franz, G. Regional Metamorphism. Enc. Geol. 2005, 407–413.
5. Gehrels, G. Detrital zircon U-Pb geochronology: current methods and new opportunities Tect. of Sed. Basins. 2012, 2, 47–62.
6. Hammerli, J.; Spandler, C.; Oliver, N.H.S. Element redistribution and mobility during upper crustal metamorphism of metasedimentary rocks: an example from the eastern Mount Lofty Ranges, South Australia. *Contrib. Miner. Pet.* **2016**, *171*, 1–21, https://doi.org/10.1007/s00410-016-1239-7.
7. Argue, J.J. Element mobility during regional metamorphism in crustal and subduction zone environments with a focus on the rare earth elements (REE). American Mineralogist, 2017, 102, 1796–1821.
8. Stepanov, A.S. A review of the geochemical changes occurring during metamorphic devolatilization of metasedimentary rocks. *Chem. Geol.* **2021**, *568*, https://doi.org/10.1016/j.chemgeo.2021.120080.
9. Brand, U.; Veizer, J. Chemical diagenesis of a multicomponent carbonatee system—l: Trace elements J. Sediment. Petrol. 1980, 50, 4, 1219–1236.
10. Reeder, R.J. 1983. Crystal chemistry of the rhombohedral carbonates.—In Reeder R. J. (ed.): Carbonates, Rev. Mineral.Geochem. 1983, 11, 1–47.
11. Veizer, J. Diagenesis of Pre-Quaternary Carbonates as Indicated by Tracer Studies. *J. Sediment. Res.* **1977**, *47*, https://doi.org/10.1306/212f71e4-2b24-11d7-8648000102c1865d.
12. Tucker, M.E.; Wright, V.P. *Carbonate Sedimentology*; Wiley: Hoboken, NJ, United States, 1990; ISBN: .
13. Komiya, T.; Hirata, T.; Kitajima, K.; Yamamoto, S.; Shibuya, T.; Sawaki, Y.; Ishikawa, T.; Shu, D.; Li, Y.; Han, J. Evolution of the composition of seawater through geologic time, and its influence on the evolution of life. *Gondwana Res.* **2008**, *14*, 159–174, https://doi.org/10.1016/j.gr.2007.10.006.
14. Zhao, M.-Y.; Zheng, Y.-F. Marine carbonate records of terrigenous input into Paleotethyan seawater: Geochemical constraints from Carboniferous limestones. *Geochim. et Cosmochim. Acta* **2014**, *141*, 508–531, https://doi.org/10.1016/j.gca.2014.07.001.
15. Melezhik, V. Strontium and carbon isotope geochemistry applied to dating of carbonate sedimentation: an example from high-grade rocks of the Norwegian Caledonides. *Precambrian Res.* **2001**, *108*, 267–292, https://doi.org/10.1016/s0301-9268(01)00135-8.
16. Tostevin, R.; Shields, G.A.; Tarbuck, G.M.; He, T.; Clarkson, M.O.; Wood, R.A. Effective use of cerium anomalies as a redox proxy in carbonate-dominated marine settings. *Chem. Geol.* **2016**, *438*, 146–162, https://doi.org/10.1016/j.chemgeo.2016.06.027.
17. Tostevin, R. Cerium Anomalies and Paleoredox (Elements in Geochemical Tracers in Earth System Science). Cambridge: Cambridge University Press, 2021.
18. Murray, W.R. Chemical criteria to identify the depositional environment of chert: general principles and applications Sed. Geol. 1994, 90, 213–232.
19. Zhang, K.-J.; Li, Q.-H.; Yan, L.-L.; Zeng, L.; Lua, L.; Zhang, Y.-X.; Hui, J.; Jin, X.; Tang, X.-C. Geochemistry of limestones deposited in various plate tectonic settings Earth Sci. Rev. 2017, 167, 27–46
20. Swart, P.K. The geochemistry of carbonate diagenesis: The past, present and future. *Sedimentology* **2015**, *62*, 1233–1304, https://doi.org/10.1111/sed.12205.
21. Fantle, M.S.; Barnes, B.D.; Lau, K.V. The Role of Diagenesis in Shaping the Geochemistry of the Marine Carbonate Record. *Annu. Rev. Earth Planet. Sci.* **2020**, *48*, 549–583, https://doi.org/10.1146/annurev-earth-073019-060021.
22. Chatalov, G. Geology of the Strandza zone in Bulgaria. Prof. Marin Drinov Publishing House of BAS, Sofia. 1990, 263 p. (in Bulgarian with an English summary).
23. Kozouharov, D.; Savov, S. Lithostratigraphy of the metamorphic Triassic of the Lissovo Graben, South Sakar, Svilengrad district. C. R. Acad. Bulg. Sci. 1996, 49, 7–8, 89–92.
24. Zagorchev, I.; Budurov, K.: Triassic geology.—In: Zagorchev, I., Ch. Dabovski, T. Nikolov (Eds.) Geology of Bulgaria. Volume II. Part 5. Mesozoic Geology. Sofia, Prof. Marin Drinov Academic Publishing House, 2009, 766 p. (in Bulgarian with an English summary).

 doi:10.20944/preprints202507.0182.v1

25. Tzankova, N.; Pristavova, P. Metamorphic evolution of garnet-bearing schists from Sakar Mountain, Southeastern Bulgaria C. R. Acad. Bulg. Sci. 2007, 60, 3, 271–278.
26. Gerdjikov, Ia.; Vangelov, D. 2025. Structure of the Southesternmost parts of the Strandzha zone, Sofia University Publishing House, 2025, 3-7 (in Bulgarian with English abstract).
27. Ivanov, Zh., 2017, Tectonics of Bulgaria. Sofia, Sofia University Publishing House, 199–224 p. (in Bulgarian with English abstract).
28. Bonev, N.; Filipov, P.; Raicheva, R.; Moritz, R. Timing and tectonic significance of Paleozoic magmatism in the Sakar unit of the Sakar-Strandzha Zone, SE Bulgaria. *Int. Geol. Rev.* **2019**, *61*, 1957–1979, https://doi.org/10.1080/00206814.2019.1575090.
29. Gerdjikov, I. 2005. Alpine metamorphism and granitoid magmatism in the Strandja Zone: New data from the Sakar Unit, SE Bulgaria Turk. J.Earth Sci. 2005, 14, 167–183.
30. Sarov, S. Lithotectonic subdivision of the metamorphic rocks in the area of Rila and Rhodope Mountains—results from geological mapping at scale 1:50 000. 2012, In: International Conference "Geological Schools of Bulgaria. The School of Prof. Z. Ivanov", 43–47.
31. Naydenov, K.; Peytcheva, I.; von Quadt, A.; Sarov, S.; Kolcheva, K.; Dimov, D. The Maritsa strike-slip shear zone between Kostenets and Krichim towns, South Bulgaria — Structural, petrographic and isotope geochronology study. *Tectonophysics* **2013**, *595-596*, 69–89, https://doi.org/10.1016/j.tecto.2012.08.005.
32. Okay, A.; Satır, M.; Tüysüz, O.; Akyüz, S.; Chen, F. The tectonics of the Strandja Massif: late-Variscan and mid-Mesozoic deformation and metamorphism in the northern Aegean. *Int. J. Earth Sci.* **2000**, *90*, 217–233, https://doi.org/10.1007/s005310000104.
33. Okay, A.I. Geology of Turkey: A Synopsus. Anschnitt 2008, 21, 19-42.
34. Sunal, G.; Satir, M.; Natal'IN, B.A.; Toraman, E. Paleotectonic Position of the Strandja Massif and Surrounding Continental Blocks Based on Zircon Pb-Pb Age Studies. *Int. Geol. Rev.* **2008**, *50*, 519–545, https://doi.org/10.2747/0020-6814.50.6.519.
35. Okay, A.I.; Nikishin, A.M. Tectonic evolution of the southern margin of Laurasia in the Black Sea region. *Int. Geol. Rev.* **2015**, *57*, 1051–1076, https://doi.org/10.1080/00206814.2015.1010609.
36. Cattò, S.; Cavazza, W.; Zattin, M.; Okay, A.I. No significant Alpine tectonic overprint on the Cimmerian Strandja Massif (SE Bulgaria and NW Turkey). *Int. Geol. Rev.* **2017**, *60*, 513–529, https://doi.org/10.1080/00206814.2017.1350604.
37. Machev, P.; Ganev, V.; Klain, L. New LA-ICP-MS U-Pb zircon dating for Strandja granitoids (SE Bulgaria): evidence for two-stage late Variscan magmatism in the internal Balkanides. *Turk. J. EARTH Sci.* **2015**, *24*, 230–248, https://doi.org/10.3906/yer-1407-21.
38. ahin, Y.S.; Aysal, N.; Güngör, Y.; Peytcheva, I.; Neubauer, F. Geochemistry and U-Pb zircon geochronology of metagranites in Istanca (Strandja) Zone, NW Pontides, Turkey: Implications for the geodynamic evolution of Cadomian orogeny, Gondwana Res. 2014, 26, 2, 755–771.
39. Natal'iN, B.A.; Sunal, G.; Gün, E.; Wang, B.; Zhiqing, Y. Precambrian to Early Cretaceous rocks of the Strandja Massif (northwestern Turkey): evolution of a long lasting magmatic arc. *Can. J. Earth Sci.* **2016**, *53*, 1312–1335, https://doi.org/10.1139/cjes-2016-0026.
40. Vladinova, Tz.; Georgieva, M. 2020, New data on the westernmost part of the Sakar unit metamorphic basement, SE Bulgaria Rev. Bulg. Geol. Soc. 2020, 81, 3, 105–107.
41. Sunal, G.; Natal'in, B.A.; Satır, M.; Toraman, E. 2006, Palaeozoic magmatic events in the Strandja Massif, NW Turkey Geodin. Acta, 2006, 19, 283–300.
42. Okay, A.I.; Satır, M.; Maluski, H.; Siyako, M.; Monie, P.; Metzger, R.; Akyüz, S. 1996, Paleo- and Neo-Tethyan events in northwestern Turkey: Geologic and geochronologic constraints, In: Yin A, and Harrison TM (editors), The tectonic evolution of Asia: Cambridge University Press United Kingdom, 1996, 420–441 p.
43. Georgiev, S.; von Quadt, A.; Heinrich, C.; Peytcheva, I.; Marchev, P. Time evolution of rifted continental arc: Integrated ID-TIMS and LA-ICPMS study of magmatic zircons from the Eastern Srednogorie, Bulgaria. Lithos, 2012, 154, 53–67.

 doi:10.20944/preprints202507.0182.v1

44. Sunal, I.; Georgiev, S.; von Quadt, A. U/Pb ID-TIMS dating of zircons from the Sakar-Strandzha Zone: New data and old questions about the Variscan orogeny in SE Europe. In: National Conference "Geosciences 2016" Sofia Bulgarian Geological Society, 71–72 p.
45. Pristavova, S.; Tzankova, N.; Gospodinov, N.; Filipov, P. 2019. Petrological study of metasomatic altered granitoids from Kanarata Deposit, Sakar Mountain, southeastern Bulgaria J. Min. Geol. Sci. 2019, 62, 53–61.
46. Sałacińska, A.; Gerdjikov, I.; Gumsley, A.; Szopa, K.; Chew, D.; Gawęda, A.; Kocjan, I. Two stages of Late Carboniferous to Triassic magmatism in the Strandja Zone of Bulgaria and Turkey. *Geol. Mag.* **2021**, *158*, 2151–2164, https://doi.org/10.1017/s0016756821000650.
47. Ekinci Şans, B.; Özdamar, Ş.; Esenli, F.; Georgiev, S. First U–Pb zircon and (U-Th)/He apatite ages of the Paleo-Tethys rocks in the Strandja Massif, NW Turkey: implications from newly identified serpentinite body Arab. J. Geosci. 2022, 15, 1257.
48. Natal'in, A.B.; Sunal, G.; Satir, M.; Toraman, E. Tectonics of the Strandja Massif, NW Turkey: History of a Long-Lived Arc at the Northern Margin of Paleo-Tethys. Turk. J. Earth Sci. 2012, 21, 755–798.
49. Kounov, A.; Gerdjikov, Ia.; Gumsley, A.; Vangelov, D.; Gumsley, P.A.; Chew, D.; Kristoffersen, M. On the presence of a Variscan metamorphism and deformation in the Sakar Unit of Strandja Massif Geol. Balc. 2024, 85, 3, 27-30.
50. Sałacińska, A.; Gerdjikov, I.; Kounov, A.; Chew, D.; Szopa, K.; Gumsley, A.; Kocjan, I.; Marciniak-Maliszewska, B.; Drakou, F. Variscan magmatic evolution of the Strandja Zone (Southeast Bulgaria and northwest Turkey) and its relationship to other north Gondwanan margin terranes. *Gondwana Res.* **2022**, *109*, 253–273, https://doi.org/10.1016/j.gr.2022.04.013.
51. Bonev, N.; Filipov, P.; Raicheva, R.; Moritz, R. Evidence of late Paleozoic and Middle Triassic magmatism in the Sakar-Strandzha Zone, SE Bulgaria, Regional geodynamic implications Int. Geol. Rev. 2021, 64, 1199–1225.
52. Aysal, N.; Şahin, S.Y.; Güngör, Y.; Peytcheva, I.; Öngen, S. Middle Permian–early Triassic magmatism in the Western Pontides, NW Turkey: Geodynamic significance for the evolution of the Paleo-Tethys. *J. Asian Earth Sci.* **2018**, *164*, 83–103, https://doi.org/10.1016/j.jseaes.2018.06.026.
53. atalov, G. Triassische kristalline Schiefer und Magmagesteine zwischen Haskovo und Dimitrovgrad C. R. Acad. Bulg. Sci. 1961, 14, 5, 503-506.
54. Chatalov, G. 1961. Triassic crystalline schists and the granites embedded in them in the area of the villages of Svetlina, Orlov dol, Gradets and Madrets (North of Sakar Mountain) Rev. Bulg. Geol. Soc. XXII, 1961, 1, 80–86. (In Bulgarian with English abstract).
55. Hagdorn, H.; Göncüoglu, M.C. Early-Middle Triassic echinoderm remains from the Istranca Massif, Turkey. *Neues Jahrb. Fur Geol. Und Palaontologie-Abhandlungen* **2007**, *246*, 235–245, https://doi.org/10.1127/0077-7749/2007/0246-0235.
56. Bonev, N.; Chiaradia, M.; Moritz, R. Strontium isotopes reveal Early Devonian to Middle Triassic carbonate sedimentation in the Sakar-Strandzha Zone, SE Bulgaria. *Int. J. Earth Sci.* **2022**, *111*, 1307–1314, https://doi.org/10.1007/s00531-022-02181-6.
57. Vladinova, Tz.; Georgieva, M.; Cherneva, Z. U-Pb datting of detrital zircons from low-grade metasedimentary rocks in the Klokotnitsa village area, SE Bulgaria, In: Proceedings of the National Conference "GEOSCIENCES 2017", Sofia, Bulgarian Geological Society, 67–68.
58. Vladinova, Tz.; Georgieva, M.; Bosse, V.; Cherneva, Z. U-Pb detrital zircons geochronology from metasedimentary rocks of the Sakar unit, Sakar-Strandzha zone, SE Bulgaria. Rev. Bulg. Geol. Soc. 2018, 79, 3, 67–68 p.
59. Filipov, P.; Bonev, N.; Raicheva, R.; Chiaradia, M.; Moritz, R. Bracheting the timing of clastic metasediments and marbles from Pirin and Sakar Mts, Bulgaria: Implication of U-Pb geochronology of detritial zircon samples and 87Sr/86Sr of carbonate rocks. In: XXI International Congress of the GBGA, Salburg, Austria, 2018, 158 p.
60. Elmas, A.; Yılmaz, İ.; Yiğitbaş, E.; Ullrich, T. A Late Jurassic–Early Cretaceous metamorphic core complex, Strandja Massif, NW Turkey. Int. J. Earth Sci. 2010, 100, 6, 1251–1263.

 doi:10.20944/preprints202507.0182.v1

61. Sunal, G.; Satir, M.; Natal'In, B.A.; Topuz, G.; Vonderschmidt, O. Metamorphism and diachronous cooling in a contractional orogen: the Strandja Massif, NW Turkey. *Geol. Mag.* **2011**, *148*, 580–596, https://doi.org/10.1017/s0016756810001020.
62. Lilov, P.; Maliakov, Y.; Balogh, K. K-Ar dating of metamorphic rocks from Strandja massif, SE Bulgaria. Geochemistry, Mineralogy and Petrology (Sofia), 2004, 41, 107–20.
63. Vladinova, Tz.; Georgieva, M.; Cherneva, Z. Geochemistry of Triassic metasediments from the area of the village of Klokotnitsa, SE Bulgaria,—In: Proceedings of the National Conference "GEOSCIENCES 2016", Sofia Bulgarian Geological Society, 77–78.
64. Chavdarova, S.; Machev, Ph. Amphibolites from Sakar Mountain—geological position and petrological features. In: National Conference "Geosciences 2017" Sofia Bulgarian Geological Society, 49–50.
65. Vladinova, Tz.; Georgieva, M.; Peytcheva, I. 2019, U-Pb geochronology and geochemistry of rutiles from metaconglomerate in the Sakar-Strandzha zone, SE Bulgaria. Rev. Bulg. Geol. Soc. 2019, 80, 3, 91–93.
66. Bonev, N.; Spikings, R.; Moritz, R. 2020, 40Ar/39Ar constraints for an early Alpine metamorphism of the Sakar unit, Sakar-Strandzha zone, Bulgaria Geol. Mag. 2020, 157, 2106–2112.
67. Gumsley, A.; Szopa, K.; Chew, D.; Gerdjikov, Ia.; Jokubauskas, P.; Marciniak-Maliszewska, B.; Drakou, F. An Early Cretaceous thermal event in the Sakar unit (Strandja Zone, SE Bulgaria/NW Turkey) revealed based on U-Pb rutile geochronology and Zr-in-rutile thermometry Lithos, 2023, 448–449.
68. Kaygısız, E.; Aysal, N.; Yağcıoğlu, K.D. Detrital zircon and rutile U–Pb dating of garnet-mica schist in the Istranca (Strandja) Massif (NW Türkiye): Mineral chemistry and metamorphic conditions. *Geochemistry* **2024**, *84*, https://doi.org/10.1016/j.chemer.2024.126172.
69. Yanev, S.; Göncüoğlu, M.C.; Gedik, I.; Lakova, I.; Boncheva, I.; Sachanski, V.; Okuyucu, C.; Özgül, N.; Timur, E.; Maliakov, Y.; et al. Stratigraphy, correlations and palaeogeography of Palaeozoic terranes of Bulgaria and NW Turkey: a review of recent data. *Geol. Soc. London, Spéc. Publ.* **2006**, *260*, 51–67, https://doi.org/10.1144/gsl.sp.2006.260.01.04.
70. Okay, A.I.; Satır, M.; Maluski, H.; Siyako, M.; Monie, P.; Metzger, R.; Akyüz, S. Paleo- and Neo-Tethyan events in northwestern Turkey: Geologic and geochronologic constraints, In: Yin A, and Harrison TM (editors), The tectonic evolution of Asia: Cambridge University Press United Kingdom, 1996, 420–441.
71. Puetz, S.J.; Spencer, C.J. Evaluating U-Pb accuracy and precision by comparing zircon ages from 12 standards using TIMS and LA-ICP-MS methods Geosystems and Geoenvironment. 2023, 2, 100177, 10.1016/j.geogeo.2022.100177, 2023.
72. atalov, A.G. Contribution to the stratigraphy and lithology of Sakar-type Triassic (Sakar Mountains, South-east Bulgaria) Rev. Bulg. Geol. Soc. XLVI, 1985, 2, 127–143.
73. Kozhuharov, D. 1968. Proterozoic complex. In: Stratigraphy of Bulgaria. (eds. V. Tsankov, H. Spasov), Science and Art, 1968, 25–62. (In Bulgarian with English abstract).
74. Boyanov, I.; Shilyafova, Zh.; Goranov, A.; Ruseva, M.; Nenov, T. Explanatory note to the Geological Map of Bulgaria with a scale of 1:100,000. Map sheet Chirpan. Committee for Geology and Mineral Resources "Geology and Geophysics" AD, 1993, 1–75.
75. Schoenherr, J.; Reuning, L.; Hallenberger, M.; Lüders, V.; Lemmens, L.; Biehl, C.B.; Lewin, A.; Leupold, M.; Wimmers, K.; Strohmenger, J.Ch. Dedolomitization: Review and case study of uncommon mesogenetic formation conditions Earth Sci. Rev. 2018, 185, 780–805.
76. Flügel, E. Microfacies of Carbonate Rocks, Analysis. Springer-Verlag, Berlin, 2010, 976.
77. Vladinova, Tz.; Georgieva, M. Metamorphic of the westernmost Triassic metasedimentary rocks in the Sakar Unit, Sakar-Strandja Zone, Bulgaria 2022, 73, 4, 353–363.
78. Taylor, S.R.; McLennan, S.M. The continental crust: its composition and evolution. United States: Web. 1985
79. McLennan, S.M.; Taylor, S.R. Th and U in sedimentary rocks: crustal evolution and sedimentary recycling. *Nature* **1980**, *285*, 621–624, https://doi.org/10.1038/285621a0.
80. McLennan, S.M.; Taylor, S.R. Sedimentary Rocks and Crustal Evolution: Tectonic Setting and Secular Trends. *J. Geol.* **1991**, *99*, 1–21, https://doi.org/10.1086/629470.
81. McLennan, S.M.; Taylor, S.R.; McCulloch, M.T; Maynard, J.B. Geochemical and Nd⊚Sr isotopic composition of deep-sea turbidites: Crustal evolution and plate tectonic associations. *Geochim. et Cosmochim. Acta* **1990**, *54*, 2015–2050, https://doi.org/10.1016/0016-7037(90)90269-q.

 doi:10.20944/preprints202507.0182.v1

82. McLennan, S.M. Rare Earth Elements in Sedimentary Rocks: Influence of Provenance and Sedimentary Processes. In: Lipin, B.R. and McKay, G.A., Eds., Geochemistry and Mineralogy of Rare Earth Elements, De Gruyter, Berlin, 1989, 169-200.
83. Tobia, F.H.; Al-Jaleel, H.S.; Rasul, A.K. Elemental and isotopic geochemistry of carbonate rocks from the Pila Spi Formation (Middle–Late Eocene), Kurdistan Region, Northern Iraq: implication for depositional environment. Arab. J. Geosci. 2020, 13, 925.
84. Ganai, A.; Rashid, A.S. 2015, Rare earth element geochemistry of the Permo-Carboniferous clastic sedimentary rocks from Spiti Region, Tethys Himalya: significance of Eu and Ce anomalies. Chin. J. Geochem. 2015, 34, 252–264.
85. Floyd, P.A.; Leveridge, B.E. Tectonic environment of the Devonian Gramscatho basin, south Cornwall: framework mode and geochemical evidence from turbiditic sandstones. *J. Geol. Soc.* **1987**, *144*, 531–542, https://doi.org/10.1144/gsjgs.144.4.0531.
86. Vladinova, Tz.; Georgieva, M.; Cherneva, Z.; Cruciani, G. Geochemistry and thermodynamic modelling of low-grade metasedimentary rocks from the Sakar-Strandja region, SE Bulgaria In: Goldschmidt Abstract, 2017, 4101.
87. Machev, Ph., 2007, Coexisting muscovite and paragonite in the metapelites from Sakar and the problem for their equilibrium Ann. Univ. Sofia, Fac. Geol. Geogr. 2007, 1, 100, 263–282.
88. Grozdanov, L.; Chatalov, A. Amphibolites from the vicinity of the village of Lessovo, the western parts of the Dervent heights, Southeast Bulgaria C. R. Acad. Bulg. Sci., 1995, 48, 5, 51–54.
89. Machev, Ph. Moissanite (SiC) from mica schists from Sakar Mtn—occurrence and petrological significance In: Bulgarian Geological Annual Scientific Conferences, Sofia, Bulgaria, 2011, 67–68.
90. Franke, W.; Ballèvre, M.; Cocks, L.; R.M., Torsvik, T.H.; Żelaźniewicz, A. Variscan Orogeny. Reference Module in Earth Systems and Environmental Sciences Encyclopedia of Geology (Second Edition), 2020, 338–349.
91. Cortesogno, L.; Gaggero, L.; Ronchi, A.; Yanev, S. Late orogenic magmatism and sedimentation within Late Carboniferous to Early Permian basins in the Balkan terrane (Bulgaria): geodynamic implications. *Int. J. Earth Sci.* **2004**, *93*, 500–520, https://doi.org/10.1007/s00531-004-0410-y.
92. Chatalov, A. 1995. Petrogtaphy, chemical composition and petrogenesis and protogenesis of upper Paleozoic and Lower Triassic metasediments from the Melnitsa-Srem Horst, Southeastern Bulgaria. Annuaire l'unversite de Sofia "St. Kliment Ohridksi" Faculte de Geologie et Geographie. 1995, 1, 88, 97–130.
93. Bonev, N.; Filipov, P.; Raicheva, R.; Moritz, R. Detrital zircon age constraints for Late Permian to Late Triassic clastic sedimentation in the northern-western Sakar-Strandzha Zone, SE Bulgaria. *Int. J. Earth Sci.* **2021**, *111*, 495–523, https://doi.org/10.1007/s00531-021-02125-6.
94. Georgieva, M., Vladinova, Tz. 2022. Geochemistry of Triassic metasediments from easternmost part of Sakar unit, Sakar-Strandzha Zone, SE Bulgaria Rev. Bulg. Geol. Soc. 2022, 83, 3 67–68.
95. Naydenov, K.A.; von Quadt, A.; Peytcheva, I.; Sarov, S.; Dimov, D. 2009, U-Pb zircon dating of metamorphic rocks in the region of Kostenets-Kozarsko villages: constraints on the tectonic evolution of the Maritsa strike-slip shear zone Rev. Bulg. Geol. Soc. 2009, 70, 1–3, 5–21.
96. Peytcheva, I.; von Quadt, A. The Palaeozoic protoliths of Central Srednogorie, Bulgaria: records in zircons frombasement rocks and Cretaceous magmatites. 5th International Symposium on Eastern Mediterranean Geology, Thessaloniki, Greece, Conference Volume, Extended abstract, 2004, T11-9.
97. Gerdzhikov, Ia.; Lazarova, A.; Kunov, A.; Vangelov, D. 2013. Highly metamorphic complexes in Bulgaria Yearb. Univ. Min. Geol. "St. Ivan Rilski" 2013, 56, I, 47–52.
98. Carrigan, C.W.; Mukasa, S.B.; Haydoutov, I.; Kolcheva, K. Age of Variscan magmatism from the Balkan sector of the orogen, central Bulgaria. *Lithos* **2005**, *82*, 125–147, https://doi.org/10.1016/j.lithos.2004.12.010.
99. Okay, A.I.; Topuz, G. Variscan orogeny in the Black Sea region. *Int. J. Earth Sci.* **2016**, *106*, 569–592, https://doi.org/10.1007/s00531-016-1395-z.
100. Pettijohn, F.; Potter, P.E.; and Siever, R. Sand and Sandstone, Springer, Berlin, 1973.

 doi:10.20944/preprints202507.0182.v1